

# Occlusion-Aware Self-Supervised Monocular 6D Object Pose Estimation

Gu Wang<sup>†</sup> , Fabian Manhardt<sup>†</sup> , Xingyu Liu , Xiangyang Ji<sup>✉</sup> , and Federico Tombari 

**Abstract**—6D object pose estimation is a fundamental yet challenging problem in computer vision. Convolutional Neural Networks (CNNs) have recently proven to be capable of predicting reliable 6D pose estimates even under monocular settings. Nonetheless, CNNs are identified as being extremely data-driven, and acquiring adequate annotations is oftentimes very time-consuming and labor intensive. To overcome this limitation, we propose a novel monocular 6D pose estimation approach by means of self-supervised learning, removing the need for real annotations. After training our proposed network fully supervised with synthetic RGB data, we leverage current trends in noisy student training and differentiable rendering to further self-supervise the model on these unsupervised real RGB(-D) samples, seeking for a visually and geometrically optimal alignment. Moreover, employing both visible and amodal mask information, our self-supervision becomes very robust towards challenging scenarios such as occlusion. Extensive evaluations demonstrate that our proposed self-supervision outperforms all other methods relying on synthetic data or employing elaborate techniques from the domain adaptation realm. Noteworthy, our self-supervised approach consistently improves over its synthetically trained baseline and often almost closes the gap towards its fully supervised counterpart. The code and models are publicly available at <https://github.com/THU-DA-6D-Pose-Group/self6dpp.git>.

**Index Terms**—6D Object Pose Estimation, Self-Supervised Learning, Differentiable Rendering, Domain Adaptation



arXiv:2203.10339v1 [cs.CV] 19 Mar 2022

## 1 INTRODUCTION

MONOCULAR estimation of the 6D pose (*i.e.* 3D translation and 3D rotation) of objects w.r.t. the camera is a long-standing problem in computer vision. Accurately localizing the 6D object pose is crucial for a wide range of real-world applications such as robotic manipulation [1], [2], [3], augmented reality [4], [5], and autonomous driving [6], [7]. Learning-based works have recently shown very promising results for the task at hand. Nonetheless, these methods are typically fed with a huge amount of data during training [8], [9]. Yet, acquiring appropriate training labels is very time-consuming and labor intensive [10], [11]. This is particularly true for 6D pose estimation, as, for each RGB-D frame, 3D CAD models need to be precisely aligned across a difficult and tedious process.

- Gu Wang, Xingyu Liu and Xiangyang Ji are with the Department of Automation, Tsinghua University, Beijing 100084, China, and also with BNRist, Beijing 100084, China. E-mail: {wangg16, liuxy21}@mails.tsinghua.edu.cn, xyji@tsinghua.edu.cn.
- Fabian Manhardt is with Google Inc., 8002 Zurich, Switzerland. E-mail: fabianmanhardt@google.com.
- Federico Tombari is with Google Inc., 8002 Zurich, Switzerland, and also with the Technical University of Munich, 80333 München, Germany. E-mail: tombari@in.tum.de.

Manuscript received 1 May 2021; revised 6 Oct. 2021; accepted 14 Dec. 2021. Date of publication 0 . 0000; date of current version 0 . 0000.

This work was supported in part by the National Key R&D Program of China under Grant 2018AAA0102801, in part by China Scholarship Council (CSC) Grant #201906210393, and in part by National Natural Science Foundation of China under Grant 61620106005.

<sup>†</sup>: Gu Wang and Fabian Manhardt have equally contributed.

<sup>✉</sup>: Xiangyang Ji is the corresponding author.

Recommended for acceptance by L. Liu, T. Hospedales, Y. LeCun, M. Long, J. Luo, W. Ouyang, M. Pietikinen, and T. Tuytelaars.

Digital Object Identifier no. 10.1109/TPAMI.2021.3136301

As a consequence, several different approaches to tackle the lacking of real labels have been proposed in literature. The most common way is to simply render a huge number of synthetic training images with tools such as OpenGL [12], [13] or Blender [14]. Via sampling of random 6D poses, large amounts of synthetic images can be simulated using the accompanying 3D CAD models. In addition, it is common to employ domain randomization to impose invariance to changing scenes [15], [16]. Thereby, images from large-scale 2D object datasets such as VOC [17] and COCO [18] are utilized as background for the rendered samples. Another line of work attempts to conduct domain adaptation by means of techniques such as GANs to translate the input from source to target domain or vice-versa [19]. Nonetheless, as these rendered images can be still effortlessly distinguished from real imagery due to low quality and physical implausibility, recent works instead investigated the use of physically-based rendering to increase quality and additionally enforce real physical constraints [3], [11]. Eventually, despite techniques based on domain adaption [19], domain randomization [20] and photorealistic rendering [11] are steadily reducing the synthetic-to-real domain gap, the performance is still far from comparable with respect to methods exploiting real imagery with 6D pose annotations during training.

Inspired by current trends from differentiable rendering [21], [22] and self-supervised learning [23], [24], we want to tackle the problem of lack of real labeled data from an entirely different viewpoint. Humans have the amazing ability to learn how to reason about the 3D world from 2D images alone. Moreover, we can even learn 3D world properties without requiring another human or *labels* in a self-supervised fashion by validating if observations of the world agree with the anticipated outcome. For instance, infants learn about *what is a 3D object* simply by observing which things move together [25]. Translating this to the task of 6D

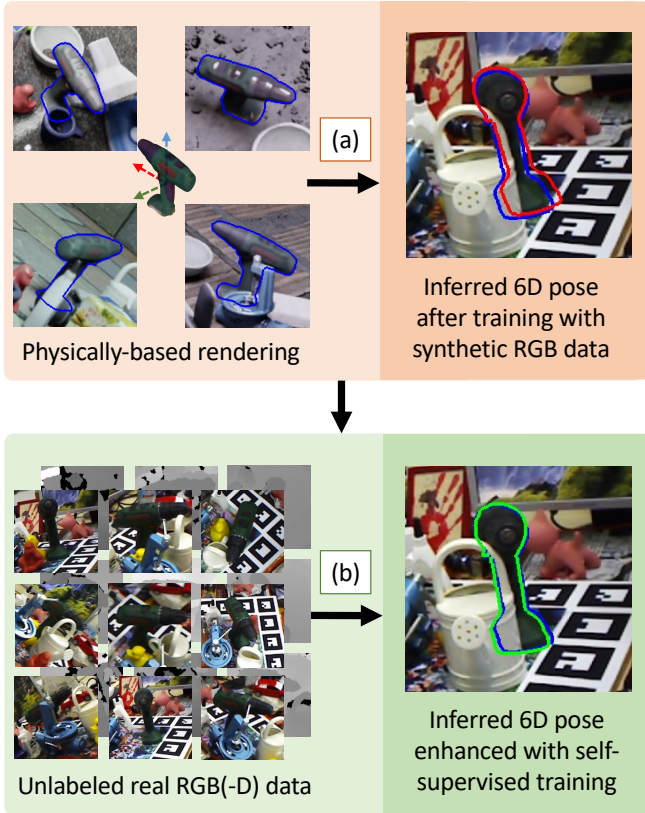


Fig. 1. *Abstract illustration* of our proposed methodology. To circumvent the use of real 6D pose annotations, we initially train our model purely on synthetic RGB data (a). Secondly, employing a large amount of unlabeled real RGB (and *optionally depth*) images (b), we significantly improve performance (right). The *blue*, *red* and *green* silhouettes respectively represent the ground-truth 6D pose, the results before and after applying our self-supervision.

pose estimation – while labeling the pose is a clear obstacle, obtaining real-world observations in form of RGB(-D) images can be easily accomplished at scale. Hence, as humans, we want the network to be capable of learning by itself from these unlabeled examples in a self-supervised fashion.

To establish supervision, the method is required to understand the 3D world solely from 2/2.5D data. Experiencing the 3D world in form of 2D images on the eye’s retina is known as *rendering* and is a very active field of research in Computer Graphics [26]. Unfortunately, most standard rendering pipelines for 3D CAD models are not differentiable as they rely on rasterization and gradients cannot be calculated for the *argmax* function. To circumvent this issue, several ideas have been recently proposed to re-establish the gradient flow for rendering [27]. Thereby, most methods either approximate a “*useful*” gradient [22], [28], or compute the analytical gradient by approximating the rasterization function itself [21], [29]. Nevertheless, to obtain such useful gradient, the rendered and real images should be fairly similar. To this end, we adopt a two-stage method as illustrated in Fig. 1. In particular, we first train our model fully-supervised on physical-based renderings [30]. We then employ unannotated RGB(-D) data to self-supervise the model on unseen real data using differentiable rendering, in an effort to diminish the synthetic-to-real domain gap.

To summarize, we make the following main technical contributions.

- We propose a self-supervised method for monocular 6D object pose estimation that leverages unsupervised RGB (or additionally with depth) images to domain adapt the model based on a differentiable learning pipeline.
- We leverage both visible and amodal object mask prediction to develop an occlusion-aware pose estimator and establish different self-supervised loss terms via visual and geometric alignment.
- We further exploit noisy student training [31] and an RGB-based deep pose refiner [32], [33] to improve the overall pose accuracy as well as its robustness to different nuisances such as occlusion and photometric changes.

To the best of our knowledge, we are the first to conduct self-supervised 6D object pose estimation from real data, without the need of real-world 6D labels. We experimentally demonstrate that the proposed self-supervised approach, which we dub Self6D++, outperforms state-of-the-art methods for monocular 6D object pose estimation trained without real annotations by a large margin.

A preliminary version of this work (Self6D) has been published as oral in ECCV 2020 [34]. In this work, we present our revised Self6D++ featuring several improvements compared to the original version. First, we replace the single-stage pose estimator by a stronger two-stage approach, notably improving over our baseline. As Yolov4 [35] provides more robust 2D detections, we can also obtain much more accurate poses using our improved version of the state-of-the-art 6D pose regressor GDR-Net [8]. Second, we introduce several important modifications to improve self-supervision under severe occlusion. In particular, the pose predictor is extended to predict both visible and full amodal masks for self-supervision. We also leverage noisy student training [31] in the self-supervised training phase to enhance robustness. We demonstrate that, differently from [34], these contributions are able to release the constraint of having depth data available during self supervision, making our method fully monocular. To this end, we employ the RGB-based deep pose refiner from [32], [33] for the teacher model so to obtain more reliable pseudo pose labels. Finally, we demonstrate the superiority of our approach through extensive experiments. Particularly, we have not only significantly improved our baseline in [34] on common benchmark datasets including LINEMOD [36], HomebrewedDB [10], Cropped LINEMOD [19] and Occluded LINEMOD [37], but also added the new evaluation for YCB-Video [38]. Moreover, compared to the initial version [34], our Self6D++ is able to produce more reliable poses under challenging scenarios w.r.t. Occluded LINEMOD and YCB-Video, which exhibit many symmetric objects undergoing significant occlusion. Throughout all benchmarks, we can almost completely fill up the gap with state-of-the-art fully-supervised methods employing real-world 6D pose labels.

## 2 RELATED WORK

We first introduce recent works in monocular 6D pose estimation. Afterwards, we discuss important methods from

differentiable rendering as they form the core of our (as well as other) self-supervised learning frameworks. We then outline other successful approaches grounded on self-supervised learning. Lastly, we take a brief look at domain adaptation in the field of 6D pose, since our method can be considered as an implicit formulation to close the synthetic-to-real domain gap.

## 2.1 Monocular 6D Pose Estimation

Traditional object pose estimation approaches rely on local image features [39], [40] or template matching [41], assuming a grayscale or RGB images as input. With the introduction of consumer RGB-D cameras, attention shifted more towards conducting object pose estimation from depth or RGB-D images. It is true that methods leveraging RGB-D data within template matching [36], point pair features [42] and learning-based methods [43], [44] often yield superior performance over RGB-only counterparts, however, they also restricted in applications as depth sensors have apparent limitations including frame rate, field of view, resolution, depth range, power consumption, and noise due to *e.g.* reflections or scattering of the laser.

Henceforth, CNN-based monocular 6D pose estimation has received a lot of attention and several very promising works have been proposed [9]. In general there are three different branches that have been extensively explored in recent history.

One major branch is grounded on establishing 2D-3D correspondences between the image and the 3D CAD model. After estimating these correspondences,  $PnP$  is commonly employed to solve for the 6D pose. For instance, BB8 [45] and YOLO6D [46] propose to employ a CNN to estimate the 2D projections of the 3D bounding box corners in image space. Similarly, SegDriven [47] and PVNet [14] also regress 2D projections of associated sparse 3D keypoints, however, both employ segmentation paired with voting to improve reliability. HybridPose [48] harnesses several intermediate representations for the 6D pose. In particular, Song *et al.* infer sparse 2D-3D correspondences together with edge vectors and symmetry correspondences to increase robustness by means of a more diverse set of features. In contrast, DPOD [49], CDPN [50], Pix2Pose [51], and EPOS [52] ascertain dense 2D-3D correspondences, rather than sparse ones. While CDPN [50] decouples the estimation of translation and rotation, Pix2Pose [51] leverages adversarial training [53] to better cope with occlusion. EPOS [52] establishes dense correspondences in an ambiguity-free manner. Using classification of fragments rather than directly regressing the correspondences, ambiguities can be deduced from the predicted distributions during inference.

Another branch of works directly regress the 6D pose. For instance, while SSD6D [15] extends SSD [54] to also classify the viewpoint and in-plane rotation, MHP [55] further adjusts SSD6D [15] to implicitly deal with ambiguities by means of multiple hypotheses. In PoseCNN [38] and DeepIM [32] the authors minimize a point matching loss. CosyPose [33] extends DeepIM [32] by the help of two cascaded iterative pose refiners for coarse registration and coarse-to-fine alignment, respectively. In addition, pose graph consistency of different static objects is enforced from multiple views to

obtain globally optimal solutions. Although inferring 2D-3D correspondences, SingleStage [56] and GDR-Net [8] directly estimate the 6D pose via learning of the  $PnP$  paradigm. Both show that learned  $PnP$  can produce more robust estimates than standard  $PnP$ , especially when the objects of interest are exposed to occlusions.

A handful of methods instead learn a pose embedding, which can be subsequently utilized for retrieval of pose. In particular, inspired by [57], [58], Sundermeyer *et al.* [20] employ an Augmented AutoEncoder (AAE) to learn latent representations for the 3D rotation. PAE [59] further exploits dense coordinates rather than RGB values as the reconstruction is thus enforced to better account for pose ambiguity. Whereas these works train separate encoders for individual objects, Sundermeyer *et al.* [60] propose to learn a shared encoder together with multiple decoders to efficiently build latent embeddings for various different objects.

Noteworthy, the majority of these methods [38], [45], [46], [47], [51] exploit annotated real data to train their models. However, labeling real data commonly comes with huge efforts in time and labor. Moreover, a shortage of sufficient real-world annotations can lead to overfitting, regardless of exploiting strategies such as Cut&Paste [10], [61]. Other works, in contrast, fully rely on synthetic data to deal with these pitfalls [20], [55]. Nonetheless, the performance falls far behind methods using real pose labels. We, hence, harness the best of both worlds. While unannotated data can be easily obtained at scale, this in combination with our self-supervision for pose is able to outperform all methods trained on synthetic data by a large margin.

## 2.2 Differentiable Rendering

Optimizing parameters through rendering has been proposed for several representations including voxel maps [62], [63], pointclouds [64], [65], implicit functions [66], [67], and 3D meshes [22], [29]. In 6D pose estimation, one usually infers the orientation and translation given a 3D CAD model, therefore, in this section we focus on non-parametric differentiable rendering methods for 3D meshes instead of parametric methods which attempt to learn the rendering function through neural networks [68]. There are two separate lines of work for differentiable rendering of 3D meshes, *i.e.*, rasterization [22], [28] as well as ray-tracing [69]. Since the latter is computationally much more expensive, we concentrate on rasterization-driven approaches here.

Rasterization involves discrete assignment operations, preventing the flow of gradients through the rendering process. A series of work have been devoted to circumvent the hard assignment in order to reestablish the gradient flow. Loper *et al.* [28] introduce the first differentiable renderer, namely OpenDR, by means of calculating the derivative of pixel values w.r.t. the 2D pixel positions within the image-space via first-order Taylor approximation. However, in OpenDR a vertex can only receive gradients from neighboring pixels within a close range of the mesh face. In NMD [22], the authors instead approximate the gradient as the potential change of the pixel's intensity w.r.t. the meshes' vertices. SoftRas [21] conducts rendering by aggregating the probabilistic contributions of each mesh triangle in relation to the rendered pixels. Consequently,

the gradients can be calculated analytically, however, with the cost of extra computation and a loss in image quality. *DIB-R* [29] further extends SoftRas [21] by considering rasterization as a combination of weighted interpolation of local mesh properties for foreground and global aggregation for background, which yields clearer images whilst still allowing occluded vertices to contribute to the optimization. In this work, we use *DIB-R* [29] since it can be considered state-of-the-art for differentiable rendering. Moreover, we extend *DIB-R* such that it also renders the accompanying depth map [34].

### 2.3 Recent Trends in Self-Supervised Learning

Self-supervised learning, *i.e.* learning despite the lack of properly labeled data, has recently enabled a large number of applications ranging from 2D image understanding all the way down to depth estimation for autonomous driving. In the core, self-supervised learning approaches implicitly learn about a specific task through solving related proxy tasks. This is commonly achieved by enforcing different constraints such as pixel consistencies across multiple views or modalities.

One prominent approach in this area is MonoDepth [23], which conducts monocular depth estimation by warping the 2D image points into another view, enforcing a minimum reprojection loss. In the following many works to extend MonoDepth have been introduced [70], [71], [72]. In visual representation learning, consistency is ensured by solving pretext tasks [73] or contrastive learning [74], [75]. Another line of works explore self-supervised learning for 3D human pose estimation, leveraging multi-view epipolar geometry [76] or imposing 2D-3D consistency via lifting and reprojection of keypoints [77]. Self-supervised learning approaches using differentiable rendering have also been proposed in the field of 3D object and human body reconstruction from single RGB images [24], [78], [79], [80], [81].

In the domain of 6D pose estimation, self-supervised learning is still a rather less explored field. Deng *et al.* [82] propose a novel self-labeling pipeline with an interactive robotic manipulator. Essentially, running several methods for 6D pose estimation, they can reliably generate precise annotations. Nonetheless, the final 6D pose estimation model is still trained fully-supervised using the acquired data. Zakharov *et al.* [66] employ differentiable rendering of implicit functions to auto-label 3D bounding boxes on KITTI3D [6]. Nevertheless, similar to Deng *et al.* [82], the final pose estimator is obtained via fully supervised training on the produced labels.

The preliminary version of our work [34] is the first method which proposes to instead directly establish self-supervision for 6D pose by enforcing visual and geometric consistencies on top of unlabeled RGB-D images on the ground of differentiable rendering. In the meanwhile, Beker *et al.* [83] harness multiple cues such as object detection, object segmentation, and depth prediction to self-supervise the model with differentiable rendering. However, a separate model needs to be optimized for each detection, which makes the approach slow due to the computational overhead for rendering and gradient computation. More recently, Sock *et al.* [84] also establish self-supervision with unlabeled images using differentiable rendering, however, only rely on RGB

data. In addition, inspired by works on self-supervised depth estimation, multi-view consistencies are employed to improve pose quality.

### 2.4 Domain Adaptation for 6D Pose Estimation

Bridging the domain gap between synthetic and real data is crucial in 6D pose estimation. Many works tackle this problem by learning a transformation to align the synthetic and real domains via Generative Adversarial Networks (GANs) [19], [85], [86] or by means of feature mapping [87]. Exemplary, Lee *et al.* [85] use a cross-cycle consistency loss based on disentangled representations to embed images onto a domain-invariant content space and a domain-specific attribute space. Rad *et al.* [87] instead translate features from a color-based pose estimator to a depth-based pose estimator.

In contrast, works from domain randomization aim at learning domain-invariant attributes. This can be accomplished harnessing random backgrounds and severe augmentations [15], [20] or employing CNNs to generate novel backgrounds and image augmentations [86]. While SSD6D [15] and AAE [20] harness COCO images as background together with various augmentations to become invariant to the domain, DeceptionNet [86] employs adversarial training to generate backgrounds and image augmentations, maximally fooling the pose estimation network.

## 3 METHODOLOGY

In this paper, we aim at conducting 6D pose estimation from monocular images without the need for a largely annotated dataset of real samples. To this end, we propose a novel method that can learn monocular pose estimation from both synthetic RGB data and unlabeled real-world RGB(-D) samples. As illustrated in Fig. 1, our approach is composed of two stages. Since generation of large-scale synthetic data can be obtained very easily at scale, we first train our model fully-supervised using synthetic RGB data only. Subsequently, to circumvent the issue of overfitting to the synthetic domain, we then enhance generalizability via self-supervision on unlabeled real-world RGB(-D) data.

Fig. 2 summarizes the proposed approach for self-supervision of monocular 6D pose estimation w.r.t. unlabeled data. We tackle the problem by means of establishing different visual and geometric constraints seeking the best alignment in terms of 6D pose. Employing the noisy student training paradigm and differentiable rendering, various visual and geometric consistencies can be established which in turn serve as strong error signal.

Contrary to [34], we make use of an occlusion-aware pose estimator built on top of GDR-Net [8]. We additionally harness visible and amodal object masks ( $M_{vis}$ ,  $M_{amodal}$ ) during self-supervision, to further improve robustness towards occlusion. Given a raw sensor RGB image  $I^S$  (and optionally the associated sensor depth image  $D^S$ ), we first extract the object of interest using an off-the-shelf object detector such as Yolov4 [35] (omitted in Fig. 2 for clarity). Thereby, the object detector and the pose estimator are both pre-trained on synthetic RGB data. From this we then initialize the teacher as well as the student pose estimators with the same weights as obtained after pre-training. While both are fed with the same

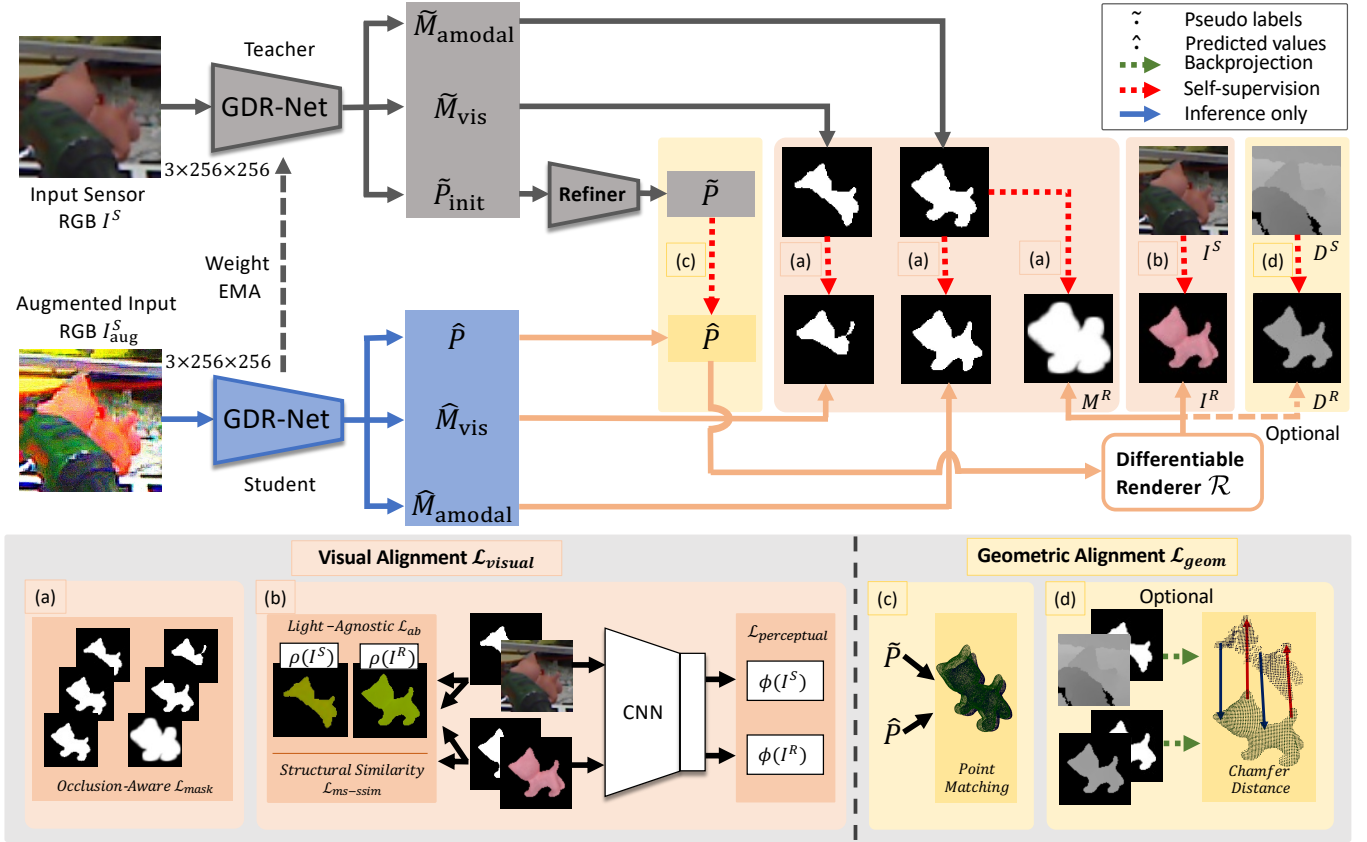


Fig. 2. *Self-supervising monocular 6D object pose estimation.* Top: After training of the Yolov4 [35] object detector (omitted for clarity), the extended GDR-Net [8] pose estimator, and the pose refiner purely with synthetic RGB images, we leverage noisy student training and differentiable rendering to self-supervise the pose estimator using a large amount of unlabeled RGB(-D) images ( $I^S$ ,  $D^S$ ). The predicted values ( $\hat{P}$ ,  $\hat{M}_{vis}$ ,  $\hat{M}_{amodal}$ ) of GDR-Net from the augmented RGB input  $I^S_{aug}$  are self-supervised by the pseudo labels ( $\tilde{P}$ ,  $\tilde{M}_{vis}$ ,  $\tilde{M}_{amodal}$ ) from the clean input RGB  $I^S$ . We also differentially render ( $\mathcal{R}$ ) the associated RGB(-D) image and probabilistic mask ( $I^R$ ,  $D^R$ ,  $M^R$ ) to register against the sensor RGB(-D) data and the pseudo amodal mask ( $I^S$ ,  $D^S$ ,  $\tilde{M}_{amodal}$ ). Bottom: We impose various constraints to visually (a and b), and geometrically (c and d) optimize the 6D object pose without requiring real pose labels.

input RGB patch  $I^S$ , the student's patch further undergoes various augmentations  $I^S_{aug}$ . Given the corresponding patch, the teacher and student then respectively predict the visible masks  $\tilde{M}_{vis}$  and  $\hat{M}_{vis}$ , amodal masks  $\tilde{M}_{amodal}$  and  $\hat{M}_{amodal}$ , and associated poses  $\tilde{P}_{init}$  and  $\hat{P}$ . Through the supervision from the teacher, the student network thus has to become agnostic to any variance as induced via augmentation. To also directly learn from the raw data, we additionally run differentiable rendering to obtain the RGB(-D) image ( $I^R$ ,  $D^R$ ) and probabilistic amodal mask  $M^R$  associated to the student's predicted pose  $\hat{P} = [\hat{R}|\hat{t}]$ , composed as the predicted rotation  $\hat{R}$  and translation  $\hat{t}$ , using the extended *DIB-R\** [29] renderer from our original work [34] with

$$\mathcal{R}(\hat{P}, K, \mathcal{M}) = (I^R, D^R, M^R). \quad (1)$$

Thereby,  $\mathcal{M}$  denotes the given 3D CAD model and  $K$  is the known camera intrinsic matrix. Moreover, leveraging a RGB-based deep pose refiner  $D_{ref}$  [32], [33], we further refine the obtained pseudo pose labels  $\tilde{P} = D_{ref}(\tilde{P}_{init})$ . Despite  $D_{ref}$  being only trained on synthetic data, the iterative process

is capable of further enhancing the quality of the pseudo label, even removing the need for depth data, which is a must in [34]. Finally, the visual and geometric alignment are established by using the pseudo labels ( $\tilde{P}$ ,  $\tilde{M}_{vis}$ ,  $\tilde{M}_{amodal}$ ) and the sensor data ( $I^S$ ,  $D^S$ ) to directly self-supervise the predicted values ( $\hat{P}$ ,  $\hat{M}_{vis}$ ,  $\hat{M}_{amodal}$ ) and through their corresponding differentially rendered data ( $I^R$ ,  $D^R$ ,  $M^R$ ).

### 3.1 Monocular Pose Estimation Under Occlusion

As we depend on differentiable rendering, inference of the 6D pose  $\hat{P}$  has to be fully differentiable in order to allow backpropagation. While it is possible to obtain gradients for  $PnP$  [88] as well as RANSAC [89], they also come with the burden of a high memory footprint and computational effort, rendering them impractical for our online learning formulation. Thus, we cannot resort to methods based on establishing 2D-3D correspondences [14], [50], [52], despite those currently dominating the field. In the first version of this work [34], we proposed a single-stage pose estimator inspired by ROI-10D [7] in order to directly estimate the rotation and translation parameters. However, especially when confronted with occlusion, the performance is far inferior to recent methods based on 2D-3D correspondences. To this end, we employ a more recent two-stage regression-based

\*We extended *DIB-R* to conduct real perspective projection and also provide the depth map fully differentially. The code has been made publicly available at <https://git.io/Self6D-Diff-Renderer>.

approach GDR-Net [8], which combines the two domains of correspondence-driven and direct regression-based methods, by utilizing dense correspondences as geometrical guidance during pose inference.

Nonetheless, the vanilla GDR-Net is still not perfectly suitable for our self-supervision, especially when the object undergoes severe occlusion. Since the rendered mask  $M^R$  is always un-occluded, the pseudo mask needs to be un-occluded as well. However, as GDR-Net only produces one output channel for the visible object mask  $M_{\text{vis}}$ , we append a second mask prediction branch for the un-occluded amodal object mask  $M_{\text{amodal}}$ . Notice that ground truth for both masks can be easily obtained from the simulator. This allows the pose estimator to better account for occlusion during self-supervision. Furthermore, we apply two additional minor changes to improve over [8]. First, we replace Faster R-CNN [90] with the faster and stronger Yolov4 detector [35]. Second, we exchange ResNet-34 [91] with a more recent ResNeSt-50 [92] backbone.

As aforementioned, we need good initial estimates to enable self-supervision. Hence, we pre-train both the object detector and the occlusion-aware pose estimator fully-supervised on simulated RGB images. Thereby, in contrast to [8], we employ the binary cross entropy loss for mask prediction. For all other losses for 6D pose and geometric features, we utilize the same objective functions as proposed in the original GDR-Net. We kindly refer the readers to [8] for more details.

### 3.2 Self-supervising Monocular 6D Pose Estimation Under Occlusion

In this section, we describe the details of visual and geometric alignment by means of noisy student training and differentiable rendering for our occlusion-aware self-supervised training. For simplicity of the following, we define all foreground and background pixels for a given mask  $M$  as

$$\text{Pos}(M) = \{(i, j) \mid \forall M(i, j) = 1\} \quad (2)$$

and

$$\text{Neg}(M) = \{(i, j) \mid \forall M(i, j) = 0\}. \quad (3)$$

**Visual Alignment for Self-Supervision.** The most intuitive way is to simply align the rendered image  $I^R$  with the sensor image  $I^S$ , deploying directly a loss on both samples. However, as the domain gap between  $I^S$  and  $I^R$  turns out to be very large, this does not work well in practice. In particular, lighting changes as well as reflection and bad reconstruction quality (especially in terms of color) often-times cause a high error despite having good pose estimates, eventually leading to divergence in the optimization. Hence, in an effort to keep the domain gap as small as possible, we impose multiple constraints measuring different domain-independent properties. In particular, we assess different visual similarities w.r.t. mask, color, image structure, and high-level content.

Since object masks are naturally domain agnostic, they can provide a particularly strong supervision. As our data is unannotated we refer to our pseudo masks ( $\widetilde{M}_{\text{vis}}$ ,  $\widetilde{M}_{\text{amodal}}$ ) for weak supervision. However, due to imperfect predicted

masks, we utilize a reweighted cross-entropy loss [93], which recalibrates the weights of positive and negative regions

$$\begin{aligned} \mathcal{L}_{\text{rwce}}(\widetilde{M}, M) := & -\frac{1}{|\text{Pos}(\widetilde{M})|} \sum_{j \in \text{Pos}(\widetilde{M})} \widetilde{M}_j \log M_j \\ & -\frac{1}{|\text{Neg}(\widetilde{M})|} \sum_{j \in \text{Neg}(\widetilde{M})} \log(1 - M_j), \end{aligned} \quad (4)$$

where  $\widetilde{M}$  is the pseudo mask and  $M$  is the corresponding predicted or rendered mask. Specifically, we harness both visible and full object masks in order to account for occlusion in visual alignment

$$\begin{aligned} \mathcal{L}_{\text{mask}} := & \lambda_1 \mathcal{L}_{\text{rwce}}(\widetilde{M}_{\text{amodal}}, M^R) \\ & + \lambda_2 \mathcal{L}_{\text{rwce}}(\widetilde{M}_{\text{amodal}}, \widehat{M}_{\text{amodal}}) \\ & + \lambda_3 \mathcal{L}_{\text{rwce}}(\widetilde{M}_{\text{vis}}, \widehat{M}_{\text{vis}}), \end{aligned} \quad (5)$$

which is balanced by  $\lambda_1$ ,  $\lambda_2$  and  $\lambda_3$ . Noticeably, Self6D only enforces a loss on the visible masks with  $\mathcal{L}_{\text{rwce}}(\widetilde{M}_{\text{vis}}, M^R)$ , turning out less robust towards occlusion compared to our formulation based on amodal masks and noisy-student training.

Although masks are not suffering from the domain gap, they discard a lot of valuable information. In particular, color information is often the only guidance to disambiguate the 6D pose, especially for geometrically simple objects. We thus resort to several techniques to mitigate the domain gap between rendered and real images.

Since the domain shift is at least partially caused by light, we attempt to decouple light prior to measuring color similarity. Let  $\rho$  denote the transformation from RGB to LAB space, additionally discarding the light channel, we evaluate color coherence on the remaining two channels according to

$$\mathcal{L}_{\text{ab}} := \frac{1}{|\text{Pos}(\widetilde{M}_{\text{vis}})|} \sum_{j \in \text{Pos}(\widetilde{M}_{\text{vis}})} \|\rho(I^S)_j \cdot \widetilde{M}_{\text{vis}_j} - \rho(I^R)_j\|_1. \quad (6)$$

We also avail various ideas from image reconstruction and domain translation, as they succumb the same dilemma. We assess the structural similarity (SSIM) in the RGB space and additionally follow the common practice to use a multi-scale variant, namely MS-SSIM [94]

$$\mathcal{L}_{\text{ms-ssim}} := 1 - \text{ms-ssim}(I^S \odot \widetilde{M}_{\text{vis}}, I^R, s). \quad (7)$$

Thereby,  $\odot$  denotes the element-wise multiplication and  $s = 5$  is the number of employed scales. For more details on MS-SSIM, we kindly refer the readers to [94].

Another common practice is to appraise the perceptual similarity [95], [96] in feature space. To this end, a pre-trained deep neural network such as AlexNet [97] is commonly employed to ensure low- and high-level similarity. We apply the perceptual loss at different levels of AlexNet. Specifically, we extract the feature maps of  $L = 5$  layers and normalize them along the channel dimension. Then we compute squared  $L_2$  distances of the normalized feature maps  $\phi^{(l)}(\cdot)$  for each layer  $l$ . We average the individual contributions spatially and sum across all layers [96]

$$\mathcal{L}_{\text{perceptual}} := \sum_{l=1}^L \text{avg}_{j \in N^{(l)}} \|\phi_j^{(l)}(I^S \odot \widetilde{M}_{\text{vis}}) - \phi_j^{(l)}(I^R)\|_2^2. \quad (8)$$

The visual alignment is then composed as the weighted sum over all four terms

$$\mathcal{L}_{visual} := \mathcal{L}_{mask} + \lambda_4 \mathcal{L}_{ab} + \lambda_5 \mathcal{L}_{ms-ssim} + \lambda_6 \mathcal{L}_{perceptual}, \quad (9)$$

with  $\lambda_4$ ,  $\lambda_5$  and  $\lambda_6$  denoting the associated loss weights.

**Geometric Alignment for Self-Supervision.** For geometric alignment we establish supervision leveraging the predicted pose  $\hat{P} = [\hat{R}|\hat{t}]$  and our pseudo pose labels  $\tilde{P}_{init} = [\tilde{R}_{init}|\tilde{t}_{init}]$ . Nonetheless, to better deal with noise due to severe occlusion, we do not directly employ a loss on top of  $\tilde{P}_{init}$  but rather use a RGB-based deep pose refiner  $D_{ref}$  [32], [33] to obtain a more robust pseudo pose label  $\tilde{P} = D_{ref}(\tilde{P}_{init})$ . Interestingly, although the refiner is also only trained with synthetic RGB data, due to its iterative nature it can still refine  $\tilde{P}_{init}$  despite external variances. We follow common procedure to utilize the point matching loss in 3D to geometrically align the 6D pose [8], [32], [38]. Thereby, the transformed model points of the prediction  $\hat{P}$  are compared with the corresponding transformed model points from  $\tilde{P}$  according to

$$\mathcal{L}_{pm} := \min_{\tilde{R} \in \mathcal{R}} \text{avg}_{x \in \mathcal{M}} \|(\hat{R}x + \hat{t}) - (\tilde{R}x + \tilde{t})\|_1. \quad (10)$$

Notice that, to account for symmetry,  $\mathcal{L}_{pm}$  is computed as the minimal loss under the set of all possible known global symmetric transformations [38]. Inspired by CosyPose [33], we also disentangle  $R$ ,  $(t_x, t_y)$  and  $t_z$  in  $\mathcal{L}_{pm}$  following Simonelli *et al.* [98], where  $t = (t_x, t_y, t_z)^T$ . Thereby, the loss is computed for each parameter separately employing the ground truth for the remaining parameters. This leads to less noisy gradients, which improves the robustness of the optimization.

When sensor depth  $D^S$  is additionally available, we can utilize it as a proxy to directly optimize the 6D pose, through geometric alignment of the target 3D model  $\mathcal{M}$  against  $D^S$ . However, as the depth map only provides information for the visible areas, holistically registration w.r.t. the transformed 3D model harms performance. Therefore, we exploit the rendered depth map to enable comparison of the visible areas only. Nevertheless, employing a loss directly on both depth maps leads to bad correspondences as the points where the masks are not intersecting cannot be matched.

Hence, we operate on the visible surface in 3D to find the best geometric alignment. We first backproject  $D^S$  and  $D^R$  using the corresponding masks  $\tilde{M}_{vis}$  and  $M^R$  to retrieve the visible pointclouds  $\mathcal{P}^S$  and  $\mathcal{P}^R$  in camera space with

$$\pi^{-1}(D, M, K) = \left\{ K^{-1} \begin{pmatrix} x_j \\ y_j \\ 1 \end{pmatrix} \cdot D_j \mid \forall j \in Pos(M) \right\}, \quad (11)$$

$$\mathcal{P}^S := \pi^{-1}(D^S, \tilde{M}_{vis}, K), \quad \mathcal{P}^R := \pi^{-1}(D^R, M^R, K). \quad (12)$$

Thereby,  $(x_j, y_j)$  denotes the 2D pixel location of  $j$  in the mask  $M$ .

Since it is infeasible to estimate direct 3D-3D correspondences between  $\mathcal{P}^S$  and  $\mathcal{P}^R$ , we refer to the chamfer distance to seek the best alignment in 3D

$$\begin{aligned} \mathcal{L}_{cham} := & \text{avg}_{p^S \in \mathcal{P}^S} \min_{p^R \in \mathcal{P}^R} \|p^S - p^R\|_2 \\ & + \text{avg}_{p^R \in \mathcal{P}^R} \min_{p^S \in \mathcal{P}^S} \|p^S - p^R\|_2. \end{aligned} \quad (13)$$

The overall geometric alignment  $\mathcal{L}_{geom}$  is respectively defined for RGB only and RGB-D as

$$\mathcal{L}_{geom}^{rgb} := \lambda_7 \mathcal{L}_{pm} \quad \mathcal{L}_{geom}^{rgb-d} := \lambda_7 \mathcal{L}_{pm} + \lambda_8 \mathcal{L}_{cham}, \quad (14)$$

where  $\lambda_7$  and  $\lambda_8$  are the corresponding loss weights.

**Overall Self-supervision.** Eventually, our self-supervision  $\mathcal{L}_{self}$  can be summarized as a simple combination of the loss terms for visual and geometric alignment in RGB as

$$\mathcal{L}_{self}^{rgb} := \mathcal{L}_{visual} + \mathcal{L}_{geom}^{rgb} \quad (15)$$

or if applicable in RGB-D as

$$\mathcal{L}_{self}^{rgb-d} := \mathcal{L}_{visual} + \mathcal{L}_{geom}^{rgb-d}. \quad (16)$$

Noteworthy, although  $\mathcal{L}_{self}^{rgb-d}$  requires depth data for self-supervised training, the learned pose estimator does still not depend on depth data during inference. Further, even when only employing RGB data alone, we can still successfully apply our self-supervision. Oppositely, the experiments from Self6D [34] have completely failed when discarding the depth channel.

## 4 EXPERIMENTS

In this section, we first describe the implementation details, employed datasets and evaluation metrics. Afterwards, we present the analysis on the quality of predicted masks and different ablations to illustrate the effectiveness of our proposed occlusion-aware self-supervision. We conclude by comparing our method with other state-of-the-art methods for 6D pose estimation and domain adaptation. For better understanding, in addition to our results, we also evaluate our method using synthetic data only and additionally employing real 6D pose labels. Since they can be considered the lower and upper bounds of our method, we refer to them OURS<sub>(LB)</sub> and OURS<sup>(UB)</sup> in the following.

### 4.1 Implementation Details

**Training Strategy.** We implemented our method using PyTorch [99] and ran all experiments on a NVIDIA TitanX GPU. All networks are trained using the Ranger optimizer [100], [101], [102]. The base learning rate is set to  $10^{-4}$  and decayed after 72% of the training phase using a cosine schedule [103]. During pre-training on simulated data, we train the 2D object detector Yolov4 [35] with a batch size of 4 for 16 epochs, our extended GDR-Net pose estimator with a batch size of 24 for 100 epochs, and the pose refiner with a batch size of 32 for 80 epochs. For the deep refiner, we train our PyTorch implementation of DeepIM [32] using the publicly available synthetic data from BOP [30] for all datasets except for YCB-Video. We instead directly utilize the public refiner from CosyPose [33] for YCB-Video, which is also pre-trained on the synthetic data from BOP [30]. During the self-supervised training stage, we train the pose estimator for another 100 epochs with a batch size of 6. The teacher network is thereby updated towards the student every 10 epochs by the exponential moving average (EMA) with a momentum of 0.999 [104]. Following standard procedure [14], [45], [48], we train the pose estimator and refiner separately for each object.

*Employed Self-supervision Hyper-Parameters.* Our overall objective function from Eq. (16) can be broken down into the following terms  $\mathcal{L}_{self}^{rgb-d} = \lambda_1 \mathcal{L}_{rwce}(\widehat{M}_{amodal}, M^R) + \lambda_2 \mathcal{L}_{rwce}(\widehat{M}_{amodal}, \widehat{M}_{amodal}) + \lambda_3 \mathcal{L}_{rwce}(\widehat{M}_{vis}, \widehat{M}_{vis}) + \lambda_4 \mathcal{L}_{ab} + \lambda_5 \mathcal{L}_{ms-ssim} + \lambda_6 \mathcal{L}_{perceptual} + \lambda_7 \mathcal{L}_{pm} + \lambda_8 \mathcal{L}_{cham}$ . We assigned the hyper-parameters such that their individual contributions are kept at a similar range as follows

hyper-parameter	$\lambda_1$	$\lambda_2$	$\lambda_3$	$\lambda_4$	$\lambda_5$	$\lambda_6$	$\lambda_7$	$\lambda_8$
value	1	1	1	0.2	1	0.15	10	{100, 0}

Notice that setting  $\lambda_8 = 0$ , the self-supervision turns into our depth free formulation as denoted in Eq. (15) for  $\mathcal{L}_{self}^{rgb}$ .

## 4.2 Datasets

### 4.2.1 Synthetic Training Data

All our networks including object detector, pose estimator and pose refiner are initially pre-trained on synthetic data. Physically-based rendering (PBR) has recently proven to be promising for improving the performance of 2D detection [11] as well as 6D pose estimation [30]. In contrast to simple OpenGL renderings [15], PBR data is more realistic and enforces physical plausibility. Therefore, in our work we utilize the publicly available PBR data from [30] together with various augmentations (*e.g.* random Gaussian noise, intensity jitter, etc. [20]) to train the models. We would like to stress that pose estimators trained on synthetic data, significantly lack in performance compared to the same networks using real pose labels, even when PBR data is employed [34]. In contrast, as emphasized in Section 4.4, inferring 2D information such as visible/amodal object masks from real data is very reliable, regardless if the model was trained on synthetic data.

### 4.2.2 Real-world Datasets

To evaluate our proposed method we leverage several commonly used real-world datasets.

*LINEMOD [36]* consists of 15 sequences, each possessing  $\approx 1.2$ k images with clutter and lighting variations. Only 13 of these provide water-tight<sup>†</sup> CAD models and we, therefore, remove the other two sequences as in other works such as SSD6D [15]. Following Brachmann *et al.* [37], we use 15% of the real data for training, however, discard the accompanying pose labels.

*HomebrewedDB [10]* is a recently proposed dataset to evaluate the 6D pose. We only employ the sequence which share three objects with LINEMOD [36] to demonstrate that we can even self-supervise the same model in a different environment.

*Occluded LINEMOD [43]* extends one sequence of LINEMOD by additionally annotating all 8 other visible objects which often undergo severe occlusion. We adopt the BOP split [9] for testing and utilize the remaining samples for our self-supervised training.

*YCB-Video [38]* is a very challenging dataset consisting of 21 objects exhibiting clutter, image noise, strong occlusion and several symmetric objects.

<sup>†</sup>When rendering these models artifacts can appear due to the holes within the mesh. In addition, the physics simulations (as done in the PBR rendering) might suffer from some undesired/unrealistic behavior.

TABLE 1  
Results of mask quality on each dataset w.r.t. mIoU (%)

Mask type	Visible	Amodal
LINEMOD [36] <sup>†</sup>	93.8	-
HomebrewedDB [10] <sup>†</sup>	93.5	-
Cropped LINEMOD [19] <sup>†</sup>	89.3	-
Occluded LINEMOD [43]	85.3	88.8
YCB-Video [38]	88.8	92.1

<sup>†</sup> For datasets with almost negligible occlusions, we only predict the visible mask and treat it as the amodal mask.

*Cropped LINEMOD [19]* is built on top of LINEMOD, including center-cropped patches of 11 different small objects in cluttered scenes portrayed in various poses. This dataset is suitable for evaluating synthetic-to-real domain adaptation and features  $\approx 110$ k rendered source images,  $\approx 10$ k real-world target images, and  $\approx 2.6$ k test images from the target domain.

## 4.3 Evaluation Metrics

We report our results referring to the common Average Distance of Distinguishable Model Points (ADD) metric [36], measuring whether the average deviation of the transformed model points  $e_{ADD}$  is less than 10% of the object’s diameter

$$e_{ADD} = \text{avg}_{x \in \mathcal{M}} \|(Rx + t) - (\widehat{R}x + \widehat{t})\|_2. \quad (17)$$

For symmetric objects (*e.g.*, Eggbox and Glue in LINEMOD) we employ the Average Distance of Indistinguishable Model Points (ADD-S) metric, which instead measures the error as the average distance to the closest model point [105]

$$e_{ADD-S} = \text{avg}_{x_2 \in \mathcal{M}} \min_{x_1 \in \mathcal{M}} \|(Rx_1 + t) - (\widehat{R}x_2 + \widehat{t})\|_2. \quad (18)$$

When evaluating on YCB-Video, we further compute the AUC (area under curve) of ADD-S/ADD(-S) by varying the distance threshold from 0cm to 10cm as in PoseCNN [38]. Thereby, ADD-S uses the symmetric metric for all objects, while ADD(-S) only uses the symmetric metric for symmetric objects. For Cropped LINEMOD, we report the average angle error following PixelDA [19].

## 4.4 Ablation Study

*Analysis on the Quality of Predicted Masks.* As self-supervision requires estimated masks of high quality from the synthetically trained model OURS<sub>(LB)</sub>, we present quantitative results for visible and amodal masks in TABLE 1. Thereby, we report the mIoU (%) between the estimated masks and ground-truth masks w.r.t. each dataset. Essentially, we can report an mIoU of no less than 85% on any dataset w.r.t. visible masks, and more than 88% for amodal masks referring to Occluded LINEMOD and YCB-Video. This shows that thanks to physically-based renderings, the predicted masks from real data are very accurate, and can be therefore used as a reliable self-supervision signal.

*Ablation of Amodal Masks on LINEMOD.* Note that for datasets like LINEMOD, HomebrewedDB and Cropped LINEMOD, the occlusion is almost negligible, hence, we



TABLE 2  
Ablation study of amodal masks on LINEMOD using the Average Recall (%) of ADD(-S) metric

	$M_{\text{amodal}}$	$M_{\text{vis}}$	ADD(-S)
OURS <sub>(LB)</sub>	✓	✓	77.2
OURS <sub>(LB)</sub>		✓	77.4
OURS	✓	✓	88.3
OURS		✓	88.5

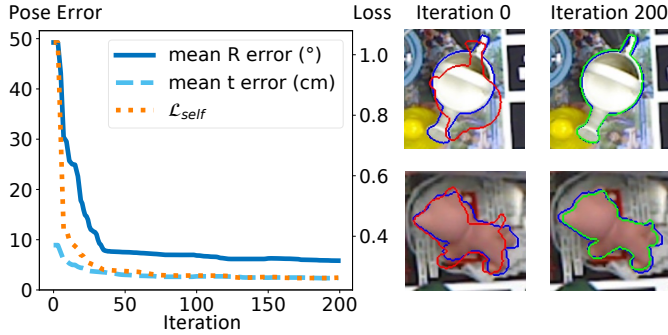


Fig. 3. *Occlusion-aware self-supervision vs. pose error.* Left: We optimize  $\mathcal{L}_{self}$  on single images from Occluded LINEMOD for 200 iterations and report the average over in total 50 images. We initialize the 6D poses with OURS<sub>(LB)</sub>. Right: Visualization of the ground-truth pose (blue) and predicted poses at iteration 0 (red) and 200 (green).

only predict the visible mask and treat it as the amodal mask. This can be verified by the ablation study on LINEMOD as shown in TABLE 2. The results of predicting “only  $M_{\text{vis}}$ ” and “both  $M_{\text{amodal}}$  and  $M_{\text{vis}}$ ” are almost the same for both the synthetically trained model OURS<sub>(LB)</sub> and the self-supervised model OURS.

*Occlusion-Aware Self-Supervision vs. Pose Error.* To demonstrate that there is indeed a high correlation between our proposed occlusion-aware self-supervision  $\mathcal{L}_{self}$  and the actual 6D pose error, we randomly draw 50 samples from Occluded LINEMOD and optimize separately on each sample, always initializing with OURS<sub>(LB)</sub>. Fig. 3 illustrates the average behavior w.r.t. loss vs. pose error at each iteration. As the loss decreases, also the pose error for both, rotation and translation, continuously declines until convergence. The accompanying qualitative images (Fig. 3, right) further support this observation, as the initial pose is clearly worse compared to the final optimized result.

*Ablation Study of Different Detectors.* In TABLE 3, we show that our method is robust to different detectors. On the BOP test set of Occluded LINEMOD, by switching the synthetically trained detector from Yolov4 [35] (AP: 64.3, AP50: 89.7, AP75: 74.2, Speed: 22.4 ms/img) to the slightly worse but much slower Faster R-CNN [90] with a ResNet101 [91] backbone ((AP: 62.4, AP50: 89.6, AP75: 74.0, Speed: 70.8 ms/img), there is only 1.2% performance drop for OURS – RGB-D. Therefore, we use Yolov4 as the base detector in all other experiments for better accuracy and efficiency.

*Effectiveness of Self-Supervision Under Occlusion.* TABLE 3 also illustrates the effectiveness of our self-supervision  $\mathcal{L}_{self}$  under occlusion referring to the BOP test set of Occluded

LINEMOD.

We first show that the noisy student training [31] strategy is very useful for establishing more robust self-supervision. When disabling data augmentation for the student’s input, almost all objects undergo a significant performance drop, and the overall average recall drops from 64.7% to 62.1%.

Note that especially geometric guidance is essential to enable self-supervision. Disabling  $\mathcal{L}_{geom}$  almost always leads to instability during training with the average recall decreasing from 52.9% to 5.1% w.r.t. ADD(-S). Interestingly, while Self6D [34] also diverged when turning off  $\mathcal{L}_{mask}$ , our new formulation exhibits more robustness which can be mostly attributed to the strong pseudo-labels produced by the teacher network together with  $D_{ref}$ .

In addition, our extension of GDR-Net to leverage amodal masks is another crucial factor for successful label-free training. When removing amodal mask  $M_{\text{amodal}}$ , the network suffers a significant drop from 64.7% to 55.1%. While  $\mathcal{L}_{visual}$  and  $\mathcal{L}_{pm}$  only have a rather small impact, the overall best results are achieved when utilizing all loss terms together. Furthermore, even when only using RGB information alone, we can present great results with 59.8%, which is equal to an absolute improvement of 6.9% over our synthetic baseline OURS<sub>(LB)</sub>.

Most importantly, we can report a compelling improvement from 52.9% to 64.7% leveraging the proposed self-supervision. Noteworthy, our self-supervision more than halves the difference between training with and without real pose labels referring to the lower and upper bounds (OURS<sub>(LB)</sub> 52.9% → OURS 64.7% → OURS<sup>(UB)</sup> 74.4%).

## 4.5 Comparison with State of the Art

In the first part of this section we present a comparison with current state-of-the-art methods in 6D pose estimation. The latter part, depicts our results in the area of domain adaptation referring to Cropped LINEMOD.

### 4.5.1 6D Pose Estimation

*Performance on LINEMOD.* In line with other works, we distinguish between training with and without real pose labels, i.e. making use of annotated real training data. Despite harnessing real data, we do not employ any pose labels and must, therefore, be classified as the latter. We want to highlight that our model can produce state-of-the-art results for training with and without labels. Referring to TABLE 4, for training using only synthetic data, OURS<sub>(LB)</sub> reveals an average recall of 77.4%, which is deliberately better than previous state-of-the-art methods like MHP [55] and DPOD [49] reporting 38.8% and 40.5%. On the other hand, as for training with real pose labels, we outperform all other recently published methods including PVNet [14] and CDPN [50] reporting a mean average recall of 91.0% w.r.t. OURS<sup>(UB)</sup>.

Notice that both of our models, RGB as well as RGB-D, come out clearly superior within all self-supervised methods reporting an average recall for 85.6% and 88.5% compared to 58.9% for Self6D and 60.6% for Sock *et al.* [84]. Moreover, whereas our method can be even successfully trained when depth is missing, Self6D [34], in contrast, fails completely when removing the depth component, decreasing from 58.9%

TABLE 3  
Ablation study on the BOP test set of Occluded LINEMOD w.r.t. the Average Recall (%) of ADD(-S)

Method	Ape	Can	Cat	Drill	Duck	Eggbox*	Glue*	Holep	Mean
Detector: Faster R-CNN [90] trained with synthetic data (AP: 62.4, AP50: 89.6, AP75: 74.0, Speed: 70.8 ms/img)									
Ours <sub>(LB)</sub>	44.6	86.9	48.0	89.5	12.8	35.0	72.9	35.0	53.1
Ours <sub>(LB)</sub> + $D_{ref}$	52.6	<b>97.5</b>	56.7	<b>97.5</b>	27.2	<b>56.1</b>	88.6	23.5	62.5
Ours – RGB-D	58.3	95.0	56.7	92.0	31.1	55.0	87.1	32.5	63.5
Detector: Yolov4 [35] trained with synthetic data (AP: 64.3, AP50: 89.7, AP75: 74.2, Speed: 22.4 ms/img)									
Ours <sub>(LB)</sub>	44.0	83.9	49.1	88.5	15.0	33.9	75.0	34.0	52.9
Ours <sub>(LB)</sub> + $D_{ref}$	53.7	97.0	60.2	96.5	27.8	51.1	<b>89.3</b>	24.5	62.5
Ours <sup>(UB)</sup>	53.7	93.5	57.3	91.5	<u>71.7</u>	<u>57.8</u>	88.6	<u>81.0</u>	<u>74.4</u>
w/o Input Augmentation	56.6	94.0	52.6	92.0	29.4	50.0	87.9	34.0	62.1
w/o $\mathcal{L}_{geom}$	0.0	0.0	0.0	19.5	0.0	7.2	1.4	13.0	5.1
w/o $M_{amodal}$	44.0	84.9	53.8	87.5	14.4	39.4	82.1	34.5	55.1
w/o $\mathcal{L}_{visual}$	58.9	95.5	56.7	93.0	32.2	48.3	87.9	33.5	63.2
w/o $\mathcal{L}_{pm}$	51.4	88.9	46.8	90.5	41.7	51.7	<b>89.3</b>	<b>54.0</b>	64.3
Ours – RGB (w/o $\mathcal{L}_{cham}$ )	57.7	95.0	52.6	90.5	26.7	45.0	87.1	23.5	59.8
Ours – RGB-D	<b>59.4</b>	96.5	<b>60.8</b>	92.0	<b>30.6</b>	51.1	88.6	38.5	<b>64.7</b>

\* denotes symmetric objects;

† The best label-free method is marked in bold, and the overall best method is underlined.

to 6.4%. We would like to stress that our proposed self-supervision is even on par with the state-of-the-art fully-supervised methods, thus, almost rendering pose labels as obsolete w.r.t. the LINEMOD dataset.

*Performance on HomebrewedDB.* In TABLE 5, we compare our method with DPOD [49] and SSD6D [15] after refinement with [16] (SSD6D+Ref.) on three objects of HomebrewedDB, which it shares with LINEMOD. Unfortunately, methods directly solving for the 6D pose always implicitly learn the camera intrinsics which degrades the performance when exposed to a new camera. 2D-3D correspondences based approaches are instead robust to camera changes as they simply run  $PnP$  using the new intrinsics. SSD6D+Ref. [16] employs contour-based pose refinement using renderings for the current hypotheses. Similarly, rendering the pose with the new intrinsics enables again easy adaptation and can even exceed DPOD and any self-supervised approach for the Bvise object. In contrast, as we directly regress the pose from a single RGB image, the performance of our Ours<sub>(LB)</sub> is worse than any other method, since we do not generalize well to the camera of HomebrewedDB. Nonetheless, we can still easily adapt to the new domain and intrinsics by only leveraging 15% of unannotated data from HomebrewedDB. In fact, we almost double the numbers for ADD for all synthetically trained methods and surpass all self-supervised approaches (i.e. Self6D [34] and Sock *et al.* [84]) by at least by 20% when only using RGB and 25% when also leveraging depth data during self-supervision. We further almost completely close the gap of over 90% between the lower and upper bounds, by pushing Ours<sub>(LB)</sub> from 3.1% to impressive 84.4% compared to Ours<sup>(UB)</sup> reporting 93.8%. Hence, our method is also very suitable for the task of domain adaption when encountering a lack of ground-truth data for the target domain.

As in our initial manuscript [34], we are again curious to understand the adaptation capabilities of our model w.r.t. the amount of real data that we expose it to. We divide the samples from HomebrewedDB into 100 images for testing

and 900 images for training. Afterwards, we repeatedly train our model with an increasing amount of data, however, always evaluating on the same test split. In Fig. 4 we illustrate the corresponding results. Harnessing only as little as 10% of the data for self-supervision, we can already almost achieve optimal performance of around 84%. This is a clear advantage over Self6D [34], who instead requires almost 50% of the data. In summary, we can achieve a faster adaptation speed with less data, while still easily exceeding Self6D.

*Performance on Occluded LINEMOD.* We additionally evaluate our method on Occluded LINEMOD in TABLE 6. As aforementioned, Occluded LINEMOD is a much more challenging dataset as many objects often undergo strong occlusion. We compare the proposed methodology with state-of-the-art methods using synthetic data only under the BOP [9] setup. Thereby, our baseline approaches Ours<sub>(LB)</sub> already clearly outperforms all other methods by a large margin. Exemplary, we exceed CosyPose [33], currently top performing method from the BOP leader board [30], by 6.2% with 52.9% compared to 46.7%. Moreover, after utilizing the remaining real RGB(-D) data for self-supervision, we again considerably enhance the performance of Ours<sub>(LB)</sub> and again

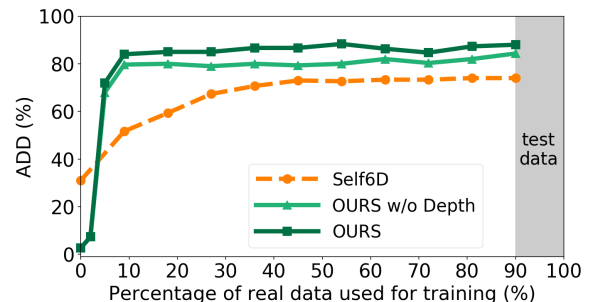


Fig. 4. Self-supervised training w.r.t. an increasing percentage of real training data on HomebrewedDB. Results are always reported on the same unseen test split.

TABLE 4  
Results on LINEMOD referring to the Average Recall (%) of ADD(-S) metric

Method	#Params (M)	Synthetic Data	Object											Mean		
			Ape	Bvise	Cam	Can	Cat	Drill	Duck	Eggbox*	Glue*	Holep	Iron		Lamp	Phone
Supervision: Syn																
AAE [20]	36.5 <sup>(d)</sup> +29.7 <sup>(p)</sup> ×13	OpenGL	4.0	20.9	30.5	35.9	17.9	24.0	4.9	81.0	45.5	17.6	32.0	60.5	33.8	31.4
MHP [55]	92.1 <sup>(p)</sup> ×12	OpenGL	11.9	66.2	22.4	59.8	26.9	44.6	8.3	55.7	54.6	15.5	60.8	-	34.4	38.8
DPOD [49] †	14.0 <sup>(p)</sup> ×13	OpenGL	35.1	59.4	15.5	48.8	28.1	59.3	25.6	51.2	34.6	17.7	84.7	45.0	20.9	40.5
DPOD+Ref. [49] †	(14.0 <sup>(p)</sup> +16.5 <sup>(r)</sup> )×13	OpenGL	52.1	64.7	22.2	77.5	56.5	65.2	49.0	62.2	38.9	25.6	98.4	58.4	33.8	54.2
OURS <sub>(LB)</sub>	96.5 <sup>(d)</sup> +42.7 <sup>(p)</sup> ×13	PBR	50.9	<b>99.4</b>	89.2	97.2	79.9	98.7	24.6	81.1	81.2	<b>41.9</b>	98.8	98.9	64.3	77.4
OURS <sub>(LB)</sub> +D <sub>ref</sub>	96.5 <sup>(d)</sup> +(42.7 <sup>(p)</sup> +37.6 <sup>(r)</sup> )×13	PBR	<u>85.8</u>	93.1	<u>99.1</u>	<u>99.8</u>	<u>91.5</u>	<u>100.0</u>	61.9	93.5	93.3	32.1	<u>100.0</u>	<u>99.1</u>	<u>94.8</u>	88.0
Supervision: Syn + Real GT																
YOLO6D [46]	50.5 <sup>(p)</sup> ×13	X	21.6	81.8	36.6	68.8	41.8	63.5	27.2	69.6	80.0	42.6	75.0	71.1	47.7	56.0
DPOD [49] †	14.0 <sup>(p)</sup> ×13	OpenGL	53.3	95.2	90.0	94.1	60.4	97.4	66.0	99.6	93.8	64.9	99.8	88.1	71.4	82.6
PVNet [14]	13.0 <sup>(p)</sup> ×13	Blender	43.6	<u>99.9</u>	86.9	95.5	79.3	96.4	52.6	99.2	95.7	81.9	98.9	99.3	92.4	86.3
CDPN [50]	41.4 <sup>(d)</sup> +113.5 <sup>(p)</sup>	OpenGL	64.4	97.8	91.7	95.9	83.8	96.2	66.8	99.7	<u>99.6</u>	<u>85.8</u>	97.9	97.9	90.8	89.9
OURS <sup>(UB)</sup>	96.5 <sup>(d)</sup> +42.7 <sup>(p)</sup> ×13	PBR	85.0	99.8	96.5	99.3	<u>93.0</u>	<u>100.0</u>	65.3	<u>99.9</u>	98.1	73.4	86.9	<u>99.6</u>	86.3	<u>91.0</u>
Supervision: Syn + Self																
Self6D [34] w/o Depth	155.1 <sup>(p)</sup>	PBR+OpenGL	0.0	10.1	3.1	0.0	0.0	7.5	0.1	33.0	0.2	0.0	5.9	20.7	2.4	6.4
Self6D [34]	155.1 <sup>(p)</sup>	PBR+OpenGL	38.9	75.2	36.9	65.6	57.9	67.0	19.6	<b>99.0</b>	94.1	16.2	77.9	68.2	50.1	58.9
Sock <i>et al.</i> [84]	60.3 <sup>(d)</sup> +25.7 <sup>(p)</sup> ×13	NMD [22]	37.6	78.6	65.5	65.6	52.5	48.8	35.1	89.2	64.5	41.5	80.9	70.7	60.5	60.6
OURS – RGB	96.5 <sup>(d)</sup> +42.7 <sup>(p)</sup> ×13	PBR	76.0	91.6	97.1	<b>99.8</b>	85.6	98.8	56.5	91.0	92.2	35.4	99.5	97.4	91.8	85.6
OURS – RGB-D	96.5 <sup>(d)</sup> +42.7 <sup>(p)</sup> ×13	PBR	75.4	94.9	97.0	99.5	86.6	98.9	<b>68.3</b>	<b>99.0</b>	<b>96.1</b>	<b>41.9</b>	99.4	98.9	94.3	<b>88.5</b>

\* denotes symmetric objects; † The numbers of DPOD [49] are different from those in their paper since they used average precision instead. The authors provided us with their results for average recall;

‡ The best label-free method is marked in bold, and the overall best method is underlined; <sup>(d)</sup> <sup>(p)</sup> <sup>(r)</sup> respectively denotes the detector, pose estimator, and refiner.

TABLE 5  
Results on HomebrewedDB

Method	#Params (M)	Synthetic Data	Object			Mean
			Bvise	Drill	Phone	
Supervision: Syn						
OURS <sub>(LB)</sub>	96.5 <sup>(d)</sup> +42.7 <sup>(p)</sup> ×3	PBR	7.1	2.2	0.1	3.1
DPOD [49] †	14.0 <sup>(p)</sup> ×3	OpenGL	52.9	37.8	7.3	32.7
SSD6D+Ref. [16] †	(92.1 <sup>(p)</sup> +5.4 <sup>(r)</sup> )×3	OpenGL	<b>82.0</b>	22.9	24.9	43.3
Supervision: Syn + Real GT						
OURS <sup>(UB)</sup>	96.5 <sup>(d)</sup> +42.7 <sup>(p)</sup> ×3	PBR	<u>98.6</u>	97.7	85.1	<u>93.8</u>
Supervision: Syn + Self						
Sock <i>et al.</i> [84]	60.3 <sup>(d)</sup> +25.7 <sup>(p)</sup> ×3	NMD [22]	57.3	46.6	41.5	52.0
Self6D [34]	155.1 <sup>(p)</sup>	PBR+OpenGL	72.1	65.1	41.8	59.7
OURS – RGB	96.5 <sup>(d)</sup> +42.7 <sup>(p)</sup> ×3	PBR	56.1	97.7	85.1	79.6
OURS – RGB-D	96.5 <sup>(d)</sup> +42.7 <sup>(p)</sup> ×3	PBR	67.1	<u>98.0</u>	<u>88.2</u>	<b>84.4</b>

† The numbers are different as in their paper since they used average precision instead. The authors provided us with their results for average recall;

‡ The best label-free method is in bold, and the overall best method is underlined; <sup>(d)</sup> <sup>(p)</sup> <sup>(r)</sup> respectively denotes the detector, pose estimator, and refiner.

outperform both Self6D [34] and Sock *et al.* [84] with a relative improvement of more than 80% or respectively 100% for RGB and RGB-D. Interestingly, despite utilizing  $D_{ref}$  [32] in our teacher model, the performance of our RGB-D version is not limited by  $D_{ref}$  (64.7% *vs.* 62.5%). However, without using depth the performance is slightly worse (59.8% *vs.* 62.5%). Nevertheless, the iterative procedure of  $D_{ref}$  makes it much slower than our direct regression for inference. Concretely, given an RGB image, our pose estimator runs with  $\approx 10$ ms, whereas  $D_{ref}$  needs additional 30ms on average.

Finally, Fig. 5 illustrates some qualitative results on Occluded LINEMOD. The poses after self-supervision (*green*) generally align much better with the ground-truth poses

(*blue*) than poses before additional self-supervision (*red*). We would like to also point out that our self-supervised model can occasionally even produce more accurate poses than some ground-truth labels (*c.f.* 2nd image from top left).

*Performance on YCB-Video.* In TABLE 7 we compare our method against state of the art [14], [32], [33], [38] on YCB-Video w.r.t. the common standard metric AUC of ADD-S/ADD(-S). In general we draw similar conclusions as for the other datasets. In particular, self-supervision either from RGB or RGB-D helps performance over the associated baseline. In addition, our approach is again almost on par with state-of-the-art methods using real pose labels for AUC of ADD(-S) with 80.0% compared to 84.5% from [33] and even

TABLE 6  
Results on the BOP test set of Occluded LINEMOD w.r.t. the Average Recall (%) of ADD(-S)

Method	#Params (M)	Synthetic Data	Object							Mean	
			Ape	Can	Cat	Drill	Duck	Eggbox*	Glue*		Holep
Supervision: Syn											
DPOD [49] †	14.0 <sup>(p)</sup> ×8	OpenGL	2.3	4.0	1.2	10.5	7.2	4.4	12.9	7.5	6.3
CDPN [50] †	55.4 <sup>(d)</sup> +13.0 <sup>(p)</sup> ×8	Blender	20.0	15.1	16.4	5.0	22.2	36.1	27.9	24.0	20.8
CDPNv2 [50] †	49.7 <sup>(d)</sup> +26.1 <sup>(p)</sup> ×8	PBR	20.6	64.8	24.0	60.0	42.2	40.0	66.4	<b>42.0</b>	45.0
CosyPose [33] †	44.0 <sup>(d)</sup> +10.7 <sup>(p)</sup> +10.7 <sup>(r)</sup>	PBR	44.0	69.9	42.1	67.5	<b>47.8</b>	24.4	60.0	17.5	46.7
OURS <sub>(LB)</sub>	96.5 <sup>(d)</sup> +42.7 <sup>(p)</sup> ×8	PBR	44.0	83.9	49.1	88.5	15.0	33.9	75.0	34.0	52.9
OURS <sub>(LB)</sub> +D <sub>ref</sub>	96.5 <sup>(d)</sup> +(42.7 <sup>(p)</sup> +37.6 <sup>(r)</sup> )×8	PBR	53.7	<u>97.0</u>	60.2	<u>96.5</u>	27.8	51.1	<u>89.3</u>	24.5	62.5
Supervision: Syn + Real GT											
OURS <sup>(UB)</sup>	96.5 <sup>(d)</sup> +42.7 <sup>(p)</sup> ×8	PBR	53.7	93.5	57.3	91.5	<u>71.7</u>	<u>57.8</u>	88.6	<u>81.0</u>	<u>74.4</u>
Supervision: Syn + Self											
Sock <i>et al.</i> [84]	60.3 <sup>(d)</sup> +25.7 <sup>(p)</sup> ×8	NMD [22]	12.0	27.5	12.0	20.5	23.0	25.1	27.0	35.0	22.8
Self6D [34]	155.1 <sup>(p)</sup>	PBR+OpenGL	13.7	43.2	18.7	32.5	14.4	<u>57.8</u>	54.3	22.0	32.1
OURS – RGB	96.5 <sup>(d)</sup> +42.7 <sup>(p)</sup> ×8	PBR	57.7	95.0	52.6	90.5	26.7	45.0	87.1	23.5	59.8
OURS – RGB-D	96.5 <sup>(d)</sup> +42.7 <sup>(p)</sup> ×8	PBR	<u>59.4</u>	96.5	<u>60.8</u>	92.0	30.6	51.1	88.6	38.5	<b>64.7</b>

\* denotes symmetric objects;

† The results are re-evaluated with ADD(-S) metric using the estimated poses for the BOP 2019 and 2020 challenges [30];

‡ The best pose label free method is marked in bold, and the overall best method is underlined; <sup>(d)</sup> <sup>(p)</sup> <sup>(r)</sup> respectively denotes the detector, pose estimator, and refiner.

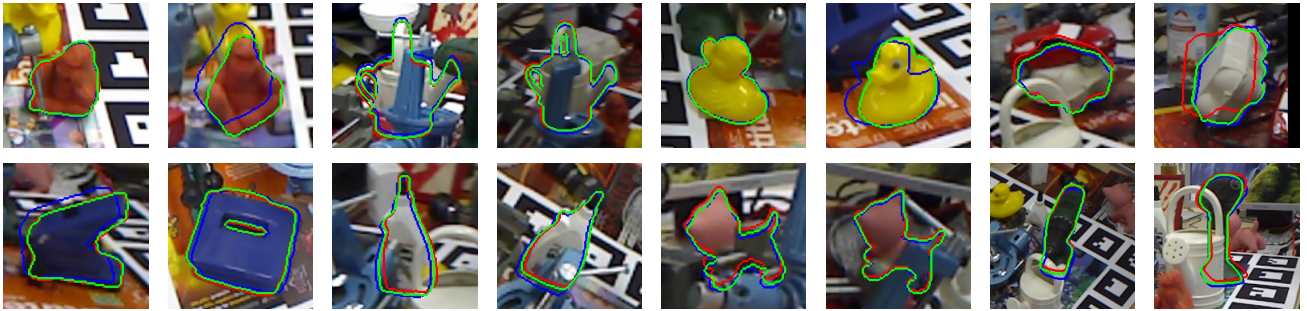


Fig. 5. Qualitative results on Occluded LINEMOD. The *Blue*, *Red* and *Green* silhouettes represent the ground-truth 6D pose, the results before and after applying our self-supervision, respectively.

TABLE 7  
Results on YCB-Video using AUC of ADD-S/ADD(-S) metrics

Method	#Params (M)	Synthetic Data	AUC of ADD-S	AUC of ADD(-S)
Supervision: Syn				
OURS <sub>(LB)</sub>	96.5 <sup>(d)</sup> +42.7 <sup>(p)</sup> ×21	PBR	89.4	77.8
OURS <sub>(LB)</sub> +D <sub>ref</sub> †	96.5 <sup>(d)</sup> +42.7 <sup>(p)</sup> ×21+10.7 <sup>(r)</sup>	PBR	90.1	79.2
Supervision: Syn + Real GT				
PoseCNN [38]	135.2 <sup>(p)</sup>	Blender	75.9	61.3
PVNet [14]	13.0 <sup>(p)</sup> ×21	Blender	-	73.4
DeepIM [32]	135.2 <sup>(p)</sup> +37.6 <sup>(r)</sup>	OpenGL	88.1	81.9
CosyPose [33]	135.2 <sup>(d)</sup> +10.7 <sup>(p)</sup> +10.7 <sup>(r)</sup>	OpenGL	89.8	<u>84.5</u>
OURS <sup>(UB)</sup>	96.5 <sup>(d)</sup> +42.7 <sup>(p)</sup> ×21	PBR	90.7	82.6
Supervision: Syn + Self				
OURS – RGB	96.5 <sup>(d)</sup> +42.7 <sup>(p)</sup> ×21	PBR	90.5	78.9
OURS – RGB-D	96.5 <sup>(d)</sup> +42.7 <sup>(p)</sup> ×21	PBR	<u>91.1</u>	<b>80.0</b>

† We employ the publicly available synthetically trained refiner from CosyPose [33] as D<sub>ref</sub>;

‡ The best pose label-free method is marked in bold, and the overall best method is underlined;

‘-’ denotes unavailable results; <sup>(d)</sup> <sup>(p)</sup> <sup>(r)</sup> respectively denotes the detector, pose estimator, and refiner.

slightly better for AUC of ADD-S with 91.1% *vs.* 90.7% from OURS<sup>(UB)</sup>. The overall improvement from self-supervision

TABLE 8  
Detailed results on YCB-Video w.r.t. AUC of ADD-S and ADD(-S)

Supervision Method	Syn				Syn + Self				Syn + Real GT	
	OURS <sub>(LB)</sub>		OURS <sub>(LB)</sub> + $D_{Ref}$		OURS – RGB		OURS – RGB-D		OURS <sup>(UB)</sup>	
	AUC of ADD-S	AUC of ADD(-S)	AUC of ADD-S	AUC of ADD(-S)	AUC of ADD-S	AUC of ADD(-S)	AUC of ADD-S	AUC of ADD(-S)	AUC of ADD-S	AUC of ADD(-S)
002_master_chef_can	<b>89.5</b>	<b>9.6</b>	81.8	8.0	86.4	8.0	88.8	8.4	<u>93.8</u>	<u>56.7</u>
003_cracker_box	94.5	85.6	<b>95.4</b>	<b>87.1</b>	93.4	83.6	94.2	84.9	<u>98.8</u>	<u>92.8</u>
004_sugar_box	93.2	82.4	<b>95.9</b>	87.6	95.1	86.5	95.8	<b>88.0</b>	<u>99.6</u>	<u>95.0</u>
005_tomato_soup_can	89.8	77.5	<b>94.4</b>	<b>84.3</b>	89.6	77.3	90.8	79.4	<u>95.4</u>	<u>90.5</u>
006_mustard_bottle	97.5	92.0	96.7	88.7	<b>98.9</b>	91.7	98.6	<b>92.7</b>	<u>100.0</u>	<u>94.7</u>
007_tuna_fish_can	96.0	86.7	95.4	85.4	96.3	86.7	<b>97.5</b>	<b>89.7</b>	<u>99.9</u>	<u>97.0</u>
008_pudding_box	96.1	89.7	84.5	71.7	96.5	89.7	<b>98.4</b>	<b>93.9</b>	63.3	42.1
009_gelatin_box	90.2	78.9	<b>94.4</b>	<b>86.4</b>	91.4	80.4	94.0	83.9	92.9	84.7
010_potted_meat_can	<b>90.4</b>	74.7	90.1	72.6	88.2	74.9	89.3	<b>75.7</b>	<u>91.1</u>	<u>78.2</u>
011_banana	<b>99.2</b>	<b>92.9</b>	97.6	90.4	97.5	91.4	98.5	91.8	93.0	80.5
019_pitcher_base	97.8	89.2	<b>99.5</b>	<b>94.7</b>	98.7	89.9	98.9	92.1	99.3	<u>98.7</u>
021_bleach_cleanser	90.5	80.3	87.9	76.8	91.9	81.7	<b>93.5</b>	<b>84.5</b>	91.2	81.9
024_bowl*	77.6	77.6	88.3	88.3	89.0	89.0	<b>89.1</b>	<b>89.1</b>	87.2	87.2
025_mug	90.1	73.1	93.9	81.0	91.8	77.4	<b>94.1</b>	<b>81.4</b>	<u>96.4</u>	<u>86.6</u>
035_power_drill	94.7	<b>84.6</b>	94.7	83.4	95.1	83.6	<b>95.2</b>	84.2	<u>99.7</u>	<u>93.6</u>
036_wood_block*	76.8	76.8	59.8	59.8	77.2	77.2	<b>78.3</b>	<b>78.3</b>	68.6	68.6
037_scissors	74.1	55.6	<b>89.2</b>	<b>75.8</b>	68.2	45.5	69.2	45.2	78.9	61.3
040_large_marker	82.9	70.5	86.5	74.8	87.3	<b>75.3</b>	<b>87.5</b>	74.6	<u>93.0</u>	<u>81.7</u>
051_large_clamp*	76.5	76.5	82.8	82.8	<b>83.8</b>	<b>83.8</b>	79.2	79.2	81.7	81.7
052_extra_large_clamp*	84.6	84.6	87.1	87.1	87.1	87.1	<b>87.3</b>	<b>87.3</b>	86.9	86.9
061_foam_brick*	94.4	94.4	95.6	95.6	<b>96.8</b>	<b>96.8</b>	95.5	95.5	94.3	94.3
Mean	89.4	77.8	90.1	79.2	90.5	78.9	<b>91.1</b>	<b>80.0</b>	90.7	<u>82.6</u>

\* denotes symmetric objects;

† The best label-free method is marked in bold, and the overall best method is underlined.

is less significant for YCB-Video as for the other datasets and only amounts to  $\approx 1\%$  or respectively  $\approx 2\%$  w.r.t. AUC of ADD-S and AUC of ADD(-S). Notice that refining the predictions with  $D_{ref}$  [33] the improvements are even smaller. This can be mostly contributed to the fact that our baseline model is already producing very strong results for the YCB-Video without requiring real pose labels as our competitors. Nonetheless, we want to stress again that our self-supervision still helps when estimating the 6D pose and produces the best results for all methods that do not employ ground-truth pose labels. In TABLE 8 we provide detailed results for each individual object.

#### 4.5.2 Domain Adaptation for Pose Estimation

Since our method is suitable for conducting synthetic to real domain adaptation, we assess transfer skills referring to the commonly used Cropped LINEMOD scenario. We self-supervise the model with the real training set from Cropped LINEMOD, and report the mean angle error on the real test set. As shown in TABLE 9, our synthetically trained model (OURS<sub>(LB)</sub>) slightly exceeds state-of-the-art methods including Self6D [34]. Essentially, our approach can successfully surpass the original model on the target domain, reducing the mean angle error from  $11.2^\circ$  to  $3.9^\circ$  (or  $4.7^\circ$  without using depth for self-supervision).

TABLE 9  
Results on Cropped LINEMOD

Method	Classification	Mean Angle
	Accuracy (%)	Error ( $^\circ$ )
PixelDA [19]	99.9	23.5
DRIT [85]	98.1	34.4
DeceptionNet [86]	95.8	51.9
Self6D [34]	100.0	15.8
OURS <sub>(LB)</sub>	100.0	11.2
OURS – RGB	100.0	4.7
OURS – RGB-D	100.0	3.9

## 5 CONCLUSION

In this work, we have introduced Self6D++, the first self-supervised 6D object pose estimation approach aimed at learning from real data without the need for 6D pose annotations. Leveraging noisy student training and differentiable rendering, we are able to enforce several visual and geometrical constraints. In addition, we proposed an occlusion-aware pose estimator to make the self-supervision more robust to challenging scenarios, exploiting both visible and amodal mask information. Moreover, compared to [34], we do not naturally depend on depth data during self-supervised training, thanks to noisy-student training and the capabilities of the RGB-based deep refiner [32], [33]. To summarize, our

method has demonstrated to remarkably reduce the gap towards the state-of-the-art for pose estimation relying on real 6D pose labels.

As future work, it would be very interesting to investigate if our self-supervision can be even applied for unseen objects or categories when no appropriate 3D CAD model is available. Another interesting aspect is to incorporate also 2D detection into our self-supervision, as this allows backpropagating the loss in an end-to-end fashion throughout both networks including Yolov4. Furthermore, the development of more lightweight and efficient self-supervised learning methods could be a very interesting and meaningful future direction.

## REFERENCES

- [1] A. Collet, M. Martinez, and S. S. Srinivasa, "The moped framework: Object recognition and pose estimation for manipulation," *Int. J. Robot. Res.*, vol. 30, no. 10, pp. 1284–1306, 2011.
- [2] M. Zhu, K. G. Derpanis, Y. Yang, S. Brahmabhatt, M. M. Zhang, C. J. Phillips, M. Lecce, and K. Daniilidis, "Single image 3d object detection and pose estimation for grasping," *Proc. IEEE Int. Conf. Robot. Automat.*, pp. 3936–3943, 2014.
- [3] J. Tremblay, T. To, B. Sundaralingam, Y. Xiang, D. Fox, and S. Birchfield, "Deep object pose estimation for semantic robotic grasping of household objects," in *Proc. Conf. Robot Learn.*, 2018, pp. 306–316.
- [4] E. Marchand, H. Uchiyama, and F. Spindler, "Pose estimation for augmented reality: a hands-on survey," *IEEE Trans. Vis. Comput. Graph.*, vol. 22, no. 12, pp. 2633–2651, 2015.
- [5] Y. Su, J. Rambach, N. Minaskan, P. Lesur, A. Pagani, and D. Stricker, "Deep multi-state object pose estimation for augmented reality assembly," in *Proc. Int. Symp. Mixed Augmented Reality Adjunct*, 2019, pp. 222–227.
- [6] A. Geiger, P. Lenz, and R. Urtasun, "Are we ready for autonomous driving? the kitti vision benchmark suite," in *Proc. IEEE/CVF Conf. Comput. Vis. Pattern Recognit.*, 2012, pp. 3354–3361.
- [7] F. Manhardt, W. Kehl, and A. Gaidon, "ROI-10D: Monocular lifting of 2d detection to 6d pose and metric shape," in *Proc. IEEE/CVF Conf. Comput. Vis. Pattern Recognit.*, 2019, pp. 2069–2078.
- [8] G. Wang, F. Manhardt, F. Tombari, and X. Ji, "GDR-Net: Geometry-guided direct regression network for monocular 6d object pose estimation," in *Proc. IEEE/CVF Conf. Comput. Vis. Pattern Recognit.*, June 2021.
- [9] T. Hodan, F. Michel, E. Brachmann, W. Kehl, A. GlentBuch, D. Kraft, B. Drost, J. Vidal, S. Ihrke, X. Zabulis et al., "BOP: Benchmark for 6d object pose estimation," in *Proc. Eur. Conf. Comput. Vis.*, 2018, pp. 19–34.
- [10] R. Kaskman, S. Zakharov, I. Shugurov, and S. Ilic, "HomebrewedDB: RGB-D dataset for 6d pose estimation of 3d objects," in *Proc. IEEE/CVF Int. Conf. Comput. Vis. Workshop*, 2019.
- [11] T. Hodaň, V. Vineet, R. Gal, E. Shalev, J. Hanzelka, T. Connell, P. Urbina, S. Sinha, and B. Guenter, "Photorealistic image synthesis for object instance detection," *Proc. IEEE Int. Conf. Image Process.*, 2019.
- [12] S. R. Richter, V. Vineet, S. Roth, and V. Koltun, "Playing for data: Ground truth from computer games," in *Proc. Eur. Conf. Comput. Vis.*, 2016, pp. 102–118.
- [13] H. Su, C. R. Qi, Y. Li, and L. J. Guibas, "Render for cnn: Viewpoint estimation in images using cnns trained with rendered 3d model views," in *Proc. IEEE/CVF Int. Conf. Comput. Vis.*, 2015, pp. 2686–2694.
- [14] S. Peng, Y. Liu, Q. Huang, X. Zhou, and H. Bao, "Pvnet: Pixel-wise voting network for 6dof pose estimation," in *Proc. IEEE/CVF Conf. Comput. Vis. Pattern Recognit.*, 2019, pp. 4561–4570.
- [15] W. Kehl, F. Manhardt, F. Tombari, S. Ilic, and N. Navab, "Ssd-6d: Making rgb-based 3d detection and 6d pose estimation great again," in *Proc. IEEE/CVF Int. Conf. Comput. Vis.*, 2017, pp. 1521–1529.
- [16] F. Manhardt, W. Kehl, N. Navab, and F. Tombari, "Deep model-based 6d pose refinement in rgb," in *Proc. Eur. Conf. Comput. Vis.*, 2018, pp. 800–815.
- [17] M. Everingham, L. Van Gool, C. K. Williams, J. Winn, and A. Zisserman, "The pascal visual object classes (voc) challenge," *Int. J. Comput. Vis.*, vol. 88, no. 2, pp. 303–338, 2010.
- [18] T.-Y. Lin, M. Maire, S. Belongie, J. Hays, P. Perona, D. Ramanan, P. Dollár, and C. L. Zitnick, "Microsoft coco: Common objects in context," in *Proc. Eur. Conf. Comput. Vis.*, 2014, pp. 740–755.
- [19] K. Bousmalis, N. Silberman, D. Dohan, D. Erhan, and D. Krishnan, "Unsupervised pixel-level domain adaptation with generative adversarial networks," in *Proc. IEEE/CVF Conf. Comput. Vis. Pattern Recognit.*, 2017, pp. 3722–3731.
- [20] M. Sundermeyer, Z.-C. Marton, M. Durner, M. Brucker, and R. Triebel, "Implicit 3d orientation learning for 6d object detection from rgb images," in *Proc. Eur. Conf. Comput. Vis.*, 2018, pp. 699–715.
- [21] S. Liu, T. Li, W. Chen, and H. Li, "Soft rasterizer: A differentiable renderer for image-based 3d reasoning," *Proc. IEEE/CVF Int. Conf. Comput. Vis.*, pp. 7708–7717, 2019.
- [22] H. Kato, Y. Ushiku, and T. Harada, "Neural 3d mesh renderer," in *Proc. IEEE/CVF Conf. Comput. Vis. Pattern Recognit.*, 2018, pp. 3907–3916.
- [23] C. Godard, O. Mac Aodha, and G. J. Brostow, "Unsupervised monocular depth estimation with left-right consistency," in *Proc. IEEE/CVF Conf. Comput. Vis. Pattern Recognit.*, 2017, pp. 270–279.
- [24] A. Kanazawa, S. Tulsiani, A. A. Efros, and J. Malik, "Learning category-specific mesh reconstruction from image collections," in *Proc. Eur. Conf. Comput. Vis.*, 2018, pp. 371–386.
- [25] E. S. Spelke, "Principles of object perception," *Cogn. Sci.*, vol. 14, no. 1, pp. 29–56, 1990.
- [26] S. Marschner and P. Shirley, *Fundamentals of Computer Graphics*. CRC Press, 2015.
- [27] H. Kato, D. Beker, M. Morariu, T. Ando, T. Matsuoka, W. Kehl, and A. Gaidon, "Differentiable rendering: A survey," *arXiv preprint arXiv:2006.12057*, 2020.
- [28] M. M. Loper and M. J. Black, "OpenDR: An approximate differentiable renderer," in *Proc. Eur. Conf. Comput. Vis.*, vol. 8695, 2014, pp. 154–169.
- [29] W. Chen, H. Ling, J. Gao, E. Smith, J. Lehtinen, A. Jacobson, and S. Fidler, "Learning to predict 3d objects with an interpolation-based differentiable renderer," in *Proc. 32nd Int. Conf. Neural Inf. Process. Syst.*, 2019, pp. 9605–9616.
- [30] T. Hodan, M. Sundermeyer, B. Drost, Y. Labbe, E. Brachmann, F. Michel, C. Rother, and J. Matas, "BOP Challenge 2020 on 6D Object Localization," *Proc. Eur. Conf. Comput. Vis. Workshop*, 2020.
- [31] Q. Xie, M.-T. Luong, E. Hovy, and Q. V. Le, "Self-training with noisy student improves imagenet classification," in *Proc. IEEE/CVF Conf. Comput. Vis. Pattern Recognit.*, June 2020.
- [32] Y. Li, G. Wang, X. Ji, Y. Xiang, and D. Fox, "DeepIM: Deep iterative matching for 6d pose estimation," *Int. J. Comput. Vis.*, pp. 1–22, 2019.
- [33] Y. Labbé, J. Carpentier, M. Aubry, and J. Sivic, "Cosypose: Consistent multi-view multi-object 6d pose estimation," in *Proc. Eur. Conf. Comput. Vis.* Springer, 2020, pp. 574–591.
- [34] G. Wang, F. Manhardt, J. Shao, X. Ji, N. Navab, and F. Tombari, "Self6d: Self-supervised monocular 6d object pose estimation," in *Proc. Eur. Conf. Comput. Vis.*, August 2020.
- [35] A. Bochkovskiy, C.-Y. Wang, and H.-Y. M. Liao, "Yolov4: Optimal speed and accuracy of object detection," *arXiv preprint arXiv:2004.10934*, 2020.
- [36] S. Hinterstoisser, V. Lepetit, S. Ilic, S. Holzer, G. Bradski, K. Konolige, and N. Navab, "Model based training, detection and pose estimation of texture-less 3d objects in heavily cluttered scenes," in *Proc. Asian Conf. Comput. Vis.*, 2012, pp. 548–562.
- [37] E. Brachmann, A. Krull, F. Michel, S. Gumhold, J. Shotton, and C. Rother, "Learning 6D object pose estimation using 3D object coordinates," in *Proc. Eur. Conf. Comput. Vis.*, 2014, pp. 536–551.
- [38] Y. Xiang, T. Schmidt, V. Narayanan, and D. Fox, "PoseCNN: A convolutional neural network for 6D object pose estimation in cluttered scenes," *Robot. Sci. Syst.*, 2018.
- [39] D. G. Lowe, "Object recognition from local scale-invariant features," in *Proc. IEEE/CVF Int. Conf. Comput. Vis.*, vol. 2, 1999, pp. 1150–1157.
- [40] A. C. Remea, M. M. Torres, and S. Srinivasa, "The moped framework: Object recognition and pose estimation for manipulation," *Int. J. Robot. Res.*, vol. 30, no. 10, pp. 1284–1306, September 2011.
- [41] S. Hinterstoisser, C. Cagniard, S. Ilic, P. Sturm, N. Navab, P. Fua, and V. Lepetit, "Gradient response maps for real-time detection of

- textureless objects," *IEEE Trans. Pattern Anal. Mach. Intell.*, vol. 34, no. 5, pp. 876–888, 2012.
- [42] S. Hinterstoisser, V. Lepetit, N. Rajkumar, and K. Konolige, "Going further with point pair features," in *Proc. Eur. Conf. Comput. Vis.* Springer, 2016, pp. 834–848.
- [43] E. Brachmann, A. Krull, F. Michel, S. Gumhold, J. Shotton, and C. Rother, "Learning 6d object pose estimation using 3d object coordinates," in *Proc. Eur. Conf. Comput. Vis.* Springer, 2014, pp. 536–551.
- [44] A. Krull, E. Brachmann, F. Michel, M. Ying Yang, S. Gumhold, and C. Rother, "Learning analysis-by-synthesis for 6D pose estimation in RGB-D images," in *Proc. IEEE/CVF Int. Conf. Comput. Vis.*, 2015, pp. 954–962.
- [45] M. Rad and V. Lepetit, "BB8: A scalable, accurate, robust to partial occlusion method for predicting the 3D poses of challenging objects without using depth," in *Proc. IEEE/CVF Int. Conf. Comput. Vis.*, 2017, pp. 3828–3836.
- [46] B. Tekin, S. N. Sinha, and P. Fua, "Real-Time Seamless Single Shot 6D Object Pose Prediction," in *Proc. IEEE/CVF Conf. Comput. Vis. Pattern Recognit.*, 2018, pp. 292–301.
- [47] Y. Hu, J. Hugonot, P. Fua, and M. Salzmann, "Segmentation-driven 6d object pose estimation," in *Proc. IEEE/CVF Conf. Comput. Vis. Pattern Recognit.*, 2019, pp. 3385–3394.
- [48] C. Song, J. Song, and Q. Huang, "Hybridpose: 6d object pose estimation under hybrid representations," in *Proc. IEEE/CVF Conf. Comput. Vis. Pattern Recognit.*, 2020, pp. 431–440.
- [49] S. Zakharov, I. Shugurov, and S. Ilic, "Dpod: 6d pose object detector and refiner," in *Proc. IEEE/CVF Int. Conf. Comput. Vis.*, 2019, pp. 1941–1950.
- [50] Z. Li, G. Wang, and X. Ji, "CDPN: Coordinates-Based Disentangled Pose Network for Real-Time RGB-Based 6-DoF Object Pose Estimation," in *Proc. IEEE/CVF Int. Conf. Comput. Vis.*, 2019, pp. 7678–7687.
- [51] K. Park, T. Patten, and M. Vincze, "Pix2pose: Pixel-wise coordinate regression of objects for 6d pose estimation," in *Proc. IEEE/CVF Int. Conf. Comput. Vis.*, 2019, pp. 7668–7677.
- [52] T. Hodan, D. Barath, and J. Matas, "Epos: Estimating 6d pose of objects with symmetries," in *Proc. IEEE/CVF Conf. Comput. Vis. Pattern Recognit.*, 2020, pp. 11703–11712.
- [53] I. Goodfellow, J. Pouget-Abadie, M. Mirza, B. Xu, D. Warde-Farley, S. Ozair, A. Courville, and J. Bengio, "Generative adversarial nets," in *Proc. 27th Int. Conf. Neural Inf. Process. Syst.*, vol. 27, 2014.
- [54] W. Liu, D. Anguelov, D. Erhan, C. Szegedy, S. Reed, C.-Y. Fu, and A. C. Berg, "SSD: Single shot multibox detector," in *Proc. Eur. Conf. Comput. Vis.*, 2016, pp. 21–37.
- [55] F. Manhardt, D. Arroyo, C. Rupprecht, B. Busam, T. Birdal, N. Navab, and F. Tombari, "Explaining the ambiguity of object detection and 6d pose from visual data," in *Proc. IEEE/CVF Int. Conf. Comput. Vis.*, 2019, pp. 6841–6850.
- [56] Y. Hu, P. Fua, W. Wang, and M. Salzmann, "Single-stage 6d object pose estimation," in *Proc. IEEE/CVF Conf. Comput. Vis. Pattern Recognit.*, 2020, pp. 2930–2939.
- [57] P. Wohlhart and V. Lepetit, "Learning descriptors for object recognition and 3d pose estimation," in *Proc. IEEE/CVF Conf. Comput. Vis. Pattern Recognit.*, 2015, pp. 3109–3118.
- [58] W. Kehl, F. Milletari, F. Tombari, S. Ilic, and N. Navab, "Deep learning of local RGB-D patches for 3D object detection and 6D pose estimation," in *Proc. Eur. Conf. Comput. Vis.*, 2016, pp. 205–220.
- [59] Z. Li and X. Ji, "Pose-guided auto-encoder and feature-based refinement for 6-dof object pose regression," in *Proc. IEEE Int. Conf. Robot. Automat.* IEEE, 2020, pp. 8397–8403.
- [60] M. Sundermeyer, M. Durner, E. Y. Puang, Z.-C. Marton, N. Vaskevicius, K. O. Arras, and R. Triebel, "Multi-path learning for object pose estimation across domains," in *Proc. IEEE/CVF Conf. Comput. Vis. Pattern Recognit.*, June 2020.
- [61] D. Dwibedi, I. Misra, and M. Hebert, "Cut, paste and learn: Surprisingly easy synthesis for instance detection," in *Proc. IEEE/CVF Int. Conf. Comput. Vis.*, 2017, pp. 1301–1310.
- [62] X. Yan, J. Yang, E. Yumer, Y. Guo, and H. Lee, "Perspective transformer nets: Learning single-view 3d object reconstruction without 3d supervision," in *Proc. 29th Int. Conf. Neural Inf. Process. Syst.*, 2016, pp. 1696–1704.
- [63] S. Tulsiani, T. Zhou, A. A. Efros, and J. Malik, "Multi-view supervision for single-view reconstruction via differentiable ray consistency," in *Proc. IEEE/CVF Conf. Comput. Vis. Pattern Recognit.*, 2017, pp. 2626–2634.
- [64] O. Wiles, G. Gkioxari, R. Szeliski, and J. Johnson, "Synsin: End-to-end view synthesis from a single image," in *Proc. IEEE/CVF Conf. Comput. Vis. Pattern Recognit.*, 2020, pp. 7467–7477.
- [65] E. Insafutdinov and A. Dosovitskiy, "Unsupervised learning of shape and pose with differentiable point clouds," in *Proc. 31st Int. Conf. Neural Inf. Process. Syst.*, 2018, pp. 2802–2812.
- [66] S. Zakharov, W. Kehl, A. Bhargava, and A. Gaidon, "Autolabeling 3d objects with differentiable rendering of sdf shape priors," in *Proc. IEEE/CVF Conf. Comput. Vis. Pattern Recognit.*, Jun. 2020.
- [67] B. Mildenhall, P. P. Srinivasan, M. Tancik, J. T. Barron, R. Ramamoorthi, and R. Ng, "Nerf: Representing scenes as neural radiance fields for view synthesis," in *Proc. Eur. Conf. Comput. Vis.*, 2020.
- [68] A. Tewari, O. Fried, J. Thies, V. Sitzmann, S. Lombardi, K. Sunkavalli, R. Martin-Brualla, T. Simon, J. Saragih, M. Nießner et al., "State of the art on neural rendering," in *Comput. Graph. Forum*, vol. 39, no. 2, 2020, pp. 701–727.
- [69] T.-M. Li, M. Aittala, F. Durand, and J. Lehtinen, "Differentiable monte carlo ray tracing through edge sampling," *ACM Trans. Graph.*, vol. 37, no. 6, pp. 1–11, 2018.
- [70] S. Pillai, R. Amrbus, and A. Gaidon, "Superdepth: Self-supervised, super-resolved monocular depth estimation," in *Proc. IEEE Int. Conf. Robot. Automat.*, 2019, pp. 9250–9256.
- [71] C. Godard, O. Mac Aodha, M. Firman, and G. J. Brostow, "Digging into self-supervised monocular depth estimation," in *Proc. IEEE/CVF Int. Conf. Comput. Vis.*, 2019, pp. 3828–3838.
- [72] V. Guizilini, R. Amrbus, S. Pillai, A. Raventos, and A. Gaidon, "3D packing for self-supervised monocular depth estimation," in *Proc. IEEE/CVF Conf. Comput. Vis. Pattern Recognit.*, 2020, pp. 2485–2494.
- [73] A. Kolesnikov, X. Zhai, and L. Beyer, "Revisiting self-supervised visual representation learning," in *Proc. IEEE/CVF Conf. Comput. Vis. Pattern Recognit.*, 2019, pp. 1920–1929.
- [74] K. He, H. Fan, Y. Wu, S. Xie, and R. Girshick, "Momentum contrast for unsupervised visual representation learning," in *Proc. IEEE/CVF Conf. Comput. Vis. Pattern Recognit.*, June 2020.
- [75] X. Chen and K. He, "Exploring simple siamese representation learning," in *Proc. IEEE/CVF Conf. Comput. Vis. Pattern Recognit.*, June 2021.
- [76] M. Kocabas, S. Karagoz, and E. Akbas, "Self-supervised learning of 3d human pose using multi-view geometry," in *Proc. IEEE/CVF Conf. Comput. Vis. Pattern Recognit.*, 2019, pp. 1077–1086.
- [77] C.-H. Chen, A. Tyagi, A. Agrawal, D. Drovner, S. Stojanov, and J. M. Rehg, "Unsupervised 3d pose estimation with geometric self-supervision," in *Proc. IEEE/CVF Conf. Comput. Vis. Pattern Recognit.*, 2019, pp. 5714–5724.
- [78] H.-Y. Tung, H.-W. Tung, E. Yumer, and K. Fragkiadaki, "Self-supervised learning of motion capture," in *Proc. 30th Int. Conf. Neural Inf. Process. Syst.*, 2017, pp. 5236–5246.
- [79] M. Omran, C. Lassner, G. Pons-Moll, P. Gehler, and B. Schiele, "Neural body fitting: Unifying deep learning and model based human pose and shape estimation," in *Proc. Int. Conf. 3D Vis.*, 2018, pp. 484–494.
- [80] T. Alldieck, M. Magnor, B. L. Bhatnagar, C. Theobalt, and G. Pons-Moll, "Learning to reconstruct people in clothing from a single rgb camera," in *Proc. IEEE/CVF Conf. Comput. Vis. Pattern Recognit.*, 2019, pp. 1175–1186.
- [81] S. Zuffi, A. Kanazawa, T. Berger-Wolf, and M. J. Black, "Three-d safari: Learning to estimate zebra pose, shape, and texture from images "in the wild", in *Proc. IEEE/CVF Int. Conf. Comput. Vis.*, 2019, pp. 5359–5368.
- [82] X. Deng, Y. Xiang, A. Mousavian, C. Eppner, T. Bretl, and D. Fox, "Self-supervised 6d object pose estimation for robot manipulation," in *Proc. IEEE Int. Conf. Robot. Automat.*, 2020.
- [83] D. Beker, H. Kato, M. A. Morariu, T. Ando, T. Matsuoka, W. Kehl, and A. Gaidon, "Monocular differentiable rendering for self-supervised 3d object detection," in *Proc. Eur. Conf. Comput. Vis.*, 2020.
- [84] J. Sock, G. Garcia-Hernando, A. Armagan, and T.-K. Kim, "Introducing pose consistency and warp-alignment for self-supervised 6d object pose estimation in color images," in *Proc. Int. Conf. 3D Vis.*, 2020, pp. 291–300.
- [85] H.-Y. Lee, H.-Y. Tseng, J.-B. Huang, M. Singh, and M.-H. Yang, "Diverse image-to-image translation via disentangled representations," in *Proc. Eur. Conf. Comput. Vis.*, 2018, pp. 35–51.
- [86] S. Zakharov, W. Kehl, and S. Ilic, "Deceptionnet: Network-driven domain randomization," in *Proc. IEEE/CVF Int. Conf. Comput. Vis.*, 2019, pp. 532–541.

- [87] M. Rad, M. Oberweger, and V. Lepetit, "Domain transfer for 3d pose estimation from color images without manual annotations," in *Proc. Asian Conf. Comput. Vis.*, 2018, pp. 69–84.
- [88] B. Chen, A. Parra, J. Cao, N. Li, and T.-J. Chin, "End-to-end learnable geometric vision by backpropagating pnp optimization," in *Proc. IEEE/CVF Conf. Comput. Vis. Pattern Recognit.*, 2020, pp. 8100–8109.
- [89] E. Brachmann, A. Krull, S. Nowozin, J. Shotton, F. Michel, S. Gumhold, and C. Rother, "Dzac-differentiable ransac for camera localization," in *Proc. IEEE/CVF Conf. Comput. Vis. Pattern Recognit.*, 2017, pp. 6684–6692.
- [90] S. Ren, K. He, R. Girshick, and J. Sun, "Faster r-cnn: Towards real-time object detection with region proposal networks," in *Proc. 28th Int. Conf. Neural Inf. Process. Syst.*, 2015, pp. 91–99.
- [91] K. He, X. Zhang, S. Ren, and J. Sun, "Deep residual learning for image recognition," in *Proc. IEEE/CVF Conf. Comput. Vis. Pattern Recognit.*, 2016, pp. 770–778.
- [92] H. Zhang, C. Wu, Z. Zhang, Y. Zhu, Z. Zhang, H. Lin, Y. Sun, T. He, J. Muller, R. Manmatha, M. Li, and A. Smola, "Resnest: Split-attention networks," *arXiv preprint arXiv:2004.08955*, 2020.
- [93] P.-T. Jiang, Q. Hou, Y. Cao, M.-M. Cheng, Y. Wei, and H.-K. Xiong, "Integral object mining via online attention accumulation," in *Proc. IEEE/CVF Int. Conf. Comput. Vis.*, 2019, pp. 2070–2079.
- [94] H. Zhao, O. Gallo, I. Frosio, and J. Kautz, "Loss functions for image restoration with neural networks," *IEEE Trans. Comput. Imag.*, vol. 3, no. 1, pp. 47–57, 2017.
- [95] J. Johnson, A. Alahi, and L. Fei-Fei, "Perceptual losses for real-time style transfer and super-resolution," in *Proc. Eur. Conf. Comput. Vis.*, 2016, pp. 694–711.
- [96] R. Zhang, P. Isola, A. A. Efros, E. Shechtman, and O. Wang, "The unreasonable effectiveness of deep features as a perceptual metric," in *Proc. IEEE/CVF Conf. Comput. Vis. Pattern Recognit.*, 2018, pp. 586–595.
- [97] A. Krizhevsky, I. Sutskever, and G. E. Hinton, "Imagenet classification with deep convolutional neural networks," in *Proc. 25th Int. Conf. Neural Inf. Process. Syst.*, 2012, pp. 1097–1105.
- [98] A. Simonelli, S. Rota Bulo, L. Porzi, M. Lopez-Antequera, and P. Kotschieder, "Disentangling Monocular 3D Object Detection," in *Proc. IEEE/CVF Int. Conf. Comput. Vis.*, 2019.
- [99] A. Paszke, S. Gross, F. Massa, A. Lerer, J. Bradbury, G. Chanan, T. Killeen, Z. Lin, N. Gimelshein, L. Antiga *et al.*, "PyTorch: An Imperative Style, High-performance Deep Learning Library," in *Proc. 32nd Int. Conf. Neural Inf. Process. Syst.*, 2019, pp. 8026–8037.
- [100] L. Liu, H. Jiang, P. He, W. Chen, X. Liu, J. Gao, and J. Han, "On the variance of the adaptive learning rate and beyond," in *Proc. Int. Conf. Learn. Representations*, April 2020.
- [101] M. Zhang, J. Lucas, J. Ba, and G. E. Hinton, "Lookahead optimizer: k steps forward, 1 step back," in *Proc. 32nd Int. Conf. Neural Inf. Process. Syst.*, 2019, pp. 9593–9604.
- [102] H. Yong, J. Huang, X. Hua, and L. Zhang, "Gradient-Centralization: A New Optimization Technique for Deep Neural Networks," in *Proc. Eur. Conf. Comput. Vis.*, 2020.
- [103] F. H. Ilya Loshchilov, "SGDR: stochastic gradient descent with warm restarts," in *Proc. Int. Conf. Learn. Representations*, 2017.
- [104] A. Tarvainen and H. Valpola, "Mean teachers are better role models: Weight-averaged consistency targets improve semi-supervised deep learning results," in *Proc. 30th Int. Conf. Neural Inf. Process. Syst.*, 2017, pp. 1195–1204.
- [105] T. Hodaň, J. Matas, and Š. Obdržálek, "On evaluation of 6d object pose estimation," *Proc. Eur. Conf. Comput. Vis. Workshop*, pp. 606–619, 2016.